Project Report
LSP-285

Selective Laser Melting of Metal Matrix Composites: FY19 Advanced Materials and Processes Line-Supported Program

E.M. Parsons
T.M. Mower

14 April 2020

Lincoln Laboratory
MASSACHUSETTS INSTITUTE OF TECHNOLOGY
LEXINGTON, MASSACHUSETTS

This material is based upon work supported by the Under Secretary of Defense for Research and Engineering under Air Force Contract No. FA8702-15-D-0001.

This report is the result of studies performed at Lincoln Laboratory, a federally funded research and development center operated by Massachusetts Institute of Technology. This material is based upon work supported by the Under Secretary of Defense for Research and Engineering under Air Force Contract No. FA8702-15-D-0001. Any opinions, findings, conclusions or recommendations expressed in this material are those of the author(s) and do not necessarily reflect the views of the Under Secretary of Defense for Research and Engineering.

Massachusetts Institute of Technology
Lincoln Laboratory

Selective Laser Melting of Metal Matrix Composites: FY19 Advanced Materials and Processes Line-Supported Program

E.M. Parsons
T.M. Mower
Group 74

Project Report LSP-285
14 April 2020

This material is based upon work supported by the Under Secretary of Defense for Research and Engineering under Air Force Contract No. FA8702-15-D-0001.

Lexington Massachusetts

This page intentionally left blank.

ABSTRACT

The capabilities of prototypes can be substantially enhanced by increasing the performance of the structural components that protect and support the payload. At MIT LL, the engineering of these components is particularly challenging because lead times are short, deformations in precision systems must be minimal, and prototypes face a range of environments, ranging from high shock and vibration loads during deployment to extreme and variable temperatures during operation. Structural performance can be improved, while simultaneously decreasing system cost and complexity, by using lightweight structural materials with a high ratio of elastic modulus to mass density, or specific stiffness. However, materials presently suitable for fabrication of prototypes all exhibit unremarkable specific stiffness. Reinforcing a ductile metal with ceramic particles results in a composite material, commonly called a metal matrix composite (MMC), that superimposes the toughness of the metal with the stiffness and thermal stability of the ceramic. Although improvements in specific stiffness of over 100% are possible, MMCs are almost never used in prototypes because they require long lead times and cannot be shaped into complex geometries with existing methods. This document describes progress toward developing aluminum matrix composites that can be processed with selective laser melting (SLM), a 3D printing method that uses a high intensity laser to consolidate thin layers of metal powder. Feedstock powders have been developed specifically for the SLM process, and laser consolidation has been conducted with an SLM testbed. The results thus far demonstrate exceptional properties at the microscale and suggest a clear path for transitioning these properties into macroscale samples and components. The ultimate goal of the program is to transfer the materials and methods to commercial SLM machines at MIT LL and other organizations, enabling materials with high specific stiffness to be used for the first time in components requiring short lead times and complex shapes.

This page intentionally left blank.

TABLE OF CONTENTS

This page intentionally left blank.

LIST OF FIGURES

LIST OF FIGURES
(Continued)

LIST OF FIGURES
(Continued)

LIST OF FIGURES

(Continued)

1. SELECTIVE LASER MELTING OF METAL MATRIX COMPOSITES: INTRODUCTION

Additive manufacturing (AM) or "3D printing" has substantially impacted numerous sectors at scales ranging from microfabrication to big area manufacturing (size of meters). Many predict that it will soon be recognized as the technology behind the third industrial revolution. It is defined by the ISO/ASTM as "the process of joining materials to make parts from 3D model data, usually layer upon layer, as opposed to subtractive and formative manufacturing methodologies." With additive manufacturing, parts of complex geometry can be built with a single machine operation and without any special masks, tooling, dies, or fixtures. Originally used primarily for fabrication of prototypes and models of design concepts, various additive manufacturing methods are presently capable of producing functional devices, components, and structures constructed from a range of material types. In fact, data published in the 2017 Wohlers Report show that the most common use of additive manufacturing is the fabrication of functional parts (33.8% of applications, and 60.6% of the market for an estimated $3.6 billion).

The first and most advanced application of 3D printing technology is the production of polymer parts. Via extrusion, photopolymerization, or fusion, parts can be fabricated from a variety of different polymers, including thermoplastics, thermosets, and polymer matrix composites. With vat polymerization, build resolution can be as good or better than it is with conventional fabrication methods (less than $1-2\,\mu$m with microstereolithography and about 50 nm with two-photon polymerization).

3D printing of metals has been much slower to develop than printing of polymers has been, but production of final parts by printing of metals is now increasing rapidly. The most common and highest resolution form of metal printing is selective laser melting (SLM), a powder bed fusion process in which selective areas of a powder bed are melted and fused with a high energy laser (Figure 1). Once fusion of a given layer is complete, the build platform is lowered, and another layer is spread or "recoated" over the platform. A similar process, selective laser sintering (SLS), can be used to fuse ceramics by sintering—not full melting. SLM has recently been adopted by MIT LL and is ideal for the production of low volumes of high value parts, typical of the defense and aerospace sectors. Heavily light-weighted parts and parts with internal channels or cavities can be manufactured, sometimes reducing to a single piece an assembly that would otherwise consist of dozens of separate components joined together. In many cases, SLM enables fabrication of parts with complex features that could not be produced at all with conventional methods.

Despite the explosive growth and many recent success stories in the additive manufacturing sector, use of AM for fabrication of critical structural components has been limited because the material properties of existing AM materials are insufficient. At MIT LL, we increasingly need high performance metals to meet the demands of prototypes that are subject to a range of thermal and mechanical loads during deployment and operation. In particular, many prototypes include components that require complex 3D shapes, high stiffness, high thermal stability, and low mass. Although

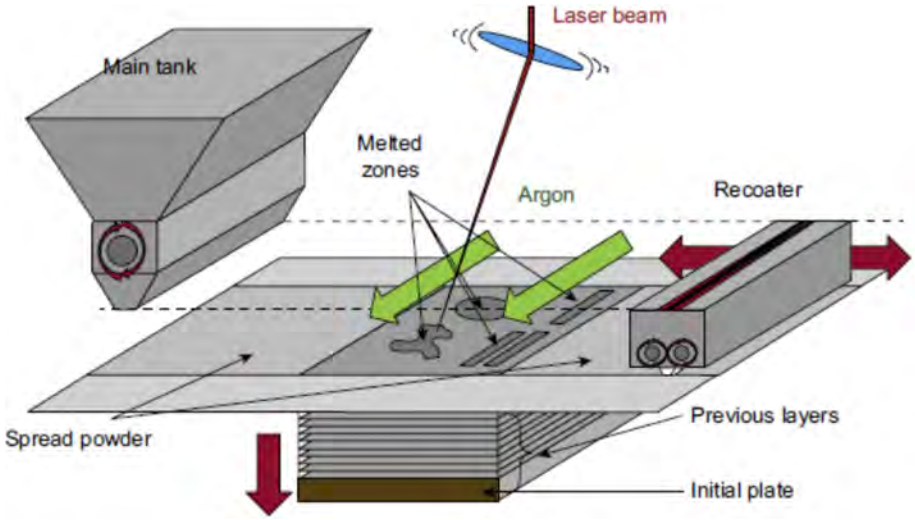

Figure 1. Schematic of the build chamber of a selective laser melting machine, showing the laser beam, build plate, powder recoater, and flow of inert gas. This example uses a hopper to deposit powder (top left), similar to the design of the micro-SLM.

selective laser melting can produce parts with unmatched geometric complexity, fabrication with SLM is presently limited to just a few alloys that exhibit unremarkable mechanical properties. For example, the only aluminum alloys widely used with SLM are AlSi10Mg and AlSi12. These alloys are designed for casting and exhibit yield strength, ductility, and fatigue strength substantially inferior to the properties of commonly used wrought alloys such as aluminum 2024, 6061, and 7075. In other cases, for a particular alloy composition, processing with SLM results in a fused material with mechanical properties that fall short of the properties of the wrought material.

In this program, we therefore seek to develop metals for SLM that exhibit properties superior to the properties of the materials that are currently available for use in prototypes. It is well known that the properties of plain metals fabricated by traditional methods can be improved dramatically by the introduction of well-dispersed ceramic particles, forming a metal matrix composite (MMC). MMCs can exhibit specific stiffness and strength nearly double those of the unreinforced metal, and the presence of the ceramic phase also improves dimensional stability and fatigue strength. However, existing MMCs are rarely used in prototypes because they require long lead times and are nearly impossible to shape into complex geometries with existing methods. The hard ceramic phase causes machining of MMCs to be slow and difficult, limiting the use of MMCs to structures that can be cast, extruded, or forged to near net shape. Fabricating MMC components with additive manufacturing would be an ideal solution, but research toward this goal has only recently begun, with few results published, and no suitable MMCs are commercially available for additive manufacturing. Here, we describe progress toward developing MMCs specifically for SLM, using

a bottom-up approach that starts by considering the elemental composition and properties of the feedstock powder.

This page intentionally left blank.

2. DEVELOPMENT OF FEEDSTOCK POWDERS

For feedstock powder, SLM requires thin, homogeneous layers of fine metal particles that are tightly packed. Not only do thin layers and small particles improve print resolution, but they are necessary to ensure adequate fusion between layers. The laser must be able both to melt fully the current layer and to penetrate into previously fused layers. Because the depth of laser penetration and the depth of the melt pool are proportional to the spot size of the laser beam, the layer thickness must scale with the diameter of the beam ($\sim 100\,\mu$m).

Unlike the few prior efforts to develop MMCs for SLM, we are designing constitutive materials and processing methods specifically for both SLM conditions and for the critical LL material requirements of stiffness and ductility. (Most prior work has focused on abrasive wear, strength, and low ceramic content, using existing MMC compositions.) For the matrix metal, we focus on aluminum alloys because they meet the common MIT LL requirements of low density, high thermal diffusivity, and good corrosion resistance. Specifically, we start with an aluminum alloy powder designed for SLM processing, AlSi10Mg. For the ceramic reinforcement, we begin with the recognition that, to form a stiff, strong, and ductile composite, particles must be evenly distributed, strongly bonded to the matrix, and small (defect-free, $\sim 1\,\mu$m). Alumina (Al_2O_3) or silicon carbide (SiC) are most often used in MMCs because they are readily available at low cost, but we determined that titanium diboride (TiB_2) is much more appropriate for SLM processing because of the nature of its chemical and physical interactions with molten aluminum.

The properties of the fused material depend, not only on the composition of the powders, but also on the properties of the powder bed. In order to minimize the porosity and surface roughness of the fused material, the uniformity and packing density of the powder bed should be maximized. Variations in layer thickness, packing density, and distributions of particle size or shape can destabilize the melt pool. These instabilities frequently lead to discontinuous or rough melt tracks that cause porosity, weak interlayer bonding, and poor surface finish. Increasing the packing density improves the thermal conductivity of the powder bed, promoting uniform heating and reducing vaporization that can cause loss of alloying elements and the formation of large pores (keyhole pores). Furthermore, with increases in packing density come also decreases in the consolidation strains that accompany melting and increases in the load bearing capacity of the unfused powder, thereby reducing residual stresses and part distortions.

2.1 RAW CONSTITUENT POWDERS

AlSi10Mg is by far the most common aluminum alloy used with SLM. In unreinforced form, the consolidated alloy exhibits good, but not exceptional, stiffness ($E \approx 69\,$GPa), strength ($\sigma_y \approx 250\,$MPa), and toughness ($e_f \approx 10\%$). The processing of AlSi10Mg by SLM is reasonably well understood: The elevated silicon content causes the melt to have high fluidity and minimizes the shrinkage that can lead to hot tearing during solidification. Furthermore, the magnesium breaks

TABLE 1

LPW AlSi10Mg SLM Powder Elemental Composition and Particle Size Distribution
($\rho_{\text{solid}} = 2.67\,\text{g/cm}^3$)

	Composition (wt%)				Particle size (μm)			Apparent
Powders	**Al**	**Si**	**Mg**	**Fe**	**d10**	**d50**	**d90**	**ρ (g/cm^3)**
LPW Standard	89.5	9.90	0.40	0.13	24.6	40.9	68.6	1.30

up the surface aluminum oxide layers and lowers the surface tension of the melt and also enables precipitation hardening by natural or artificial aging.

Gas atomized AlSi10Mg powders from several different powder manufacturers were considered (Valimet, ECKA Granules, and LPW). Gas atomization is commonly used to manufacture powders for powder bed fusion because it produces reasonably spherical particles at an affordable cost. The elemental compositions of the powders were nearly identical, but the morphology of the powders differed substantially. Of the standard SLM powders with $d_{50} \sim 35\,\mu$m, the powder from Valimet was the most spherical and smallest in diameter, while the powder from LPW was the least spherical and largest in diameter. The plain powders all exhibit apparent densities in the range of 1.3–1.4 g/cm^3, with apparent density increasing with increasing particle size and sphericity. Small and angular particles pack poorly compared to large, spherical particles because of the effects of interparticle interference, friction, and cohesive forces. We chose the powder from LPW because it exhibited consistent properties and performance, and it is readily available in the U.S.A. (Table 1 and Figure 2a).

Titanium diboride was chosen as the ceramic reinforcement because of its excellent physical properties and inertness when in contact with molten aluminum at high temperatures. TiB_2 is nearly eight times stiffer than aluminum ($E = 530{-}565\,\text{GPa}$) and over ten times as hard (25–35 GPa Vickers). It has a high melting point ($T_\text{m} = 2790{-}3225\,^\circ\text{C}$), low solubility in liquid aluminum at high temperature (1.21×10^{-8} at 960 °C), and very low reactivity with aluminum, minimizing the risk of forming brittle intermetallic phases. Furthermore TiB_2 and aluminum have physical properties that favor particle engulfment, epitaxial growth, wetting, and strong interfacial bonding. (The Hamaker constant of TiB_2 characterizing the nature of the repulsive van der Waals forces is close to that of molten aluminum, and the two materials have crystallographic orientation relationships that minimize the solid-particle interfacial energy.) We purchased several different powders from U.S. Research Nanomaterials and H.C. Starck (Table 2) with particle sizes in the range of 1–10 μm—about an order of magnitude smaller than the size of the AlSi10Mg particles.

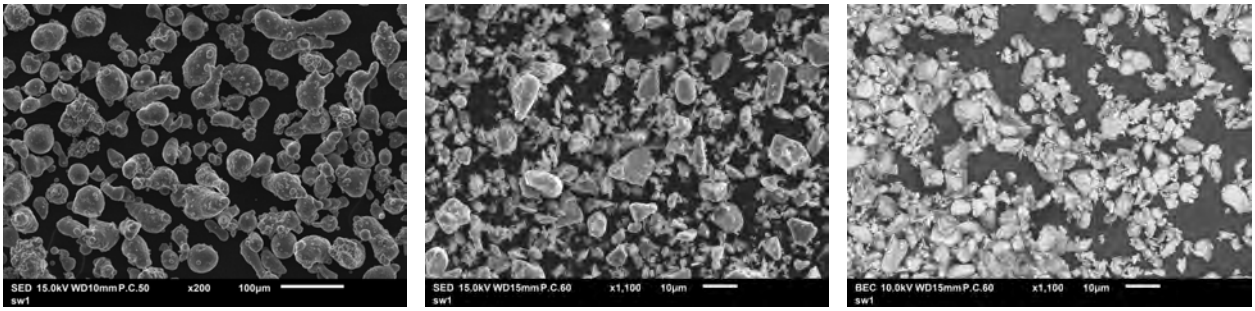

(a) (b) (c)

Figure 2. SEM images of raw, commercial powders from various manufacturers. (a) Gas atomized AlSi10Mg, showing occasional rod-shaped particles. (b) Titanium diboride microparticles from U.S. Research Nanomaterials. (c) Titanium diboride microparticles from H.C. Starck. The ceramic particles from both suppliers exhibit angular shapes, with sizes in the range of 1–10 µm.

The various powders were chosen so that we could investigate the effect of particle size distribution (PSD), shape, and elemental composition (namely, carbon and oxygen content). Manufactured by crushing or grinding, the TiB_2 particles are angular and faceted but approximately equiaxed in shape (Figure 2). The $0.2-5.0\,\mu$m particles from H.C. Starck, in particular, exhibit a strong tendency to agglomerate because cohesive forces exceed gravitational forces at this particle size. We selected the TiB_2 powder from U.S. Research Nanomaterials because it mixed well with the AlSi10Mg powder and its particles are nearly equiaxed in shape (Figure 2b).

2.2 PRODUCTION OF COMPOSITE POWDERS

In this section, we describe the development of powders that are a composite of AlSi10Mg and TiB_2. The first goal was to produce powders that are a homogeneous mixture of the two materials in order to maximize the likelihood that the ceramic will be evenly distributed in the consolidated composite. Agglomeration of the TiB_2 particles must be avoided because brittle fracture of MMCs often initiates within clusters of reinforcements, where high levels of hydrostatic stress cause voids to form in the metal. The second goal was to produce composite powders with good flow characteristics so that thin, uniform layers of the powder can be spread over the build plate of the SLM machine.

2.2.1 Method

Aluminum and ceramic powders were gently dry mixed in a shaker mixer (Glen Mills Turbula T2F). The powders were first dried for 16 h at 80 °C. Then, the mixer's stainless steel vial was loaded under argon with the AlSi10Mg and TiB_2 powders, and the powder was mixed for 16 h at

TABLE 2

Summary of Titanium Diboride Physical Characteristics

	Composition (wt%)						Particle size (μm)		
Powders	**Ti**	**B**	**C**	**H**	**O**	**Fe**	**d10**	**d50**	**d90**
U.S. Nano	> 67.5	> 30.50	0.22	0.030	1.25	< 0.2	3.7	6.9	12.6
H.C. Starck D	Bal	30.6	0.22	0.019	0.84	0.03	3.5	6.7	12.0
H.C. Starck F	Bal	31.1	0.1	-	0.9	0.0	0.7	2.9	5.0

60 rpm. We handled, mixed, and stored the powders under argon in order to prevent the formation of excessive oxides that can cause defects in laser consolidated materials. Mixes were produced at several weight fractions of TiB_2, w=10–30%, and all blends exhibited even distribution of the two phases. Furthermore, there was no evidence that the aluminum particles were deformed by the mixing process. (Figure 3 shows typical mixed powders.)

Composite powders were also manufactured by mechanically alloying in a planetary ball mill (Fritsch PULVERISETTE 5 Premium). Mechanical alloying is a high energy, solid state process that can produce homogeneous mixtures of multiple materials at or below the microscale. In a planetary mill, two steel or ceramic vials are loaded with the powders to be alloyed and balls made from a material identical to that of the vials. The vials are then secured to a disc that rotates at high speed during milling, while the vials spin in the opposite direction about their own axes at an angular speed of about twice the rate of disc rotation (Figure 4a). The impacts between the balls and the inner walls of the vials cold weld and fracture intervening particles such that the final milled powder is composed of particles that are each a composite or alloy of the starting powders. Here, as illustrated in Figure 4b, the goals were to create ceramic-reinforced aluminum particles that are equiaxed and similar in size to the starting aluminum powder. We hypothesized that the uniform mixture of aluminum and ceramic, with intimate contact even in the solid state, would ensure distribution and wetting of the ceramic particles during laser consolidation. Furthermore, the monodisperse particle size distribution that is typical of mechanically alloyed powders should optimize the flow characteristics of the composite powder.

Mechanical alloying is characterized by numerous process variables that control the properties of the alloyed powder. For given disk and vial diameters, the mass of each ball and the speed of the mill determine the theoretical energy per impact, E_b, while the size of each ball and the fill ratio of the vial primarily affect the efficiency of the process. A combination of these parameters determines

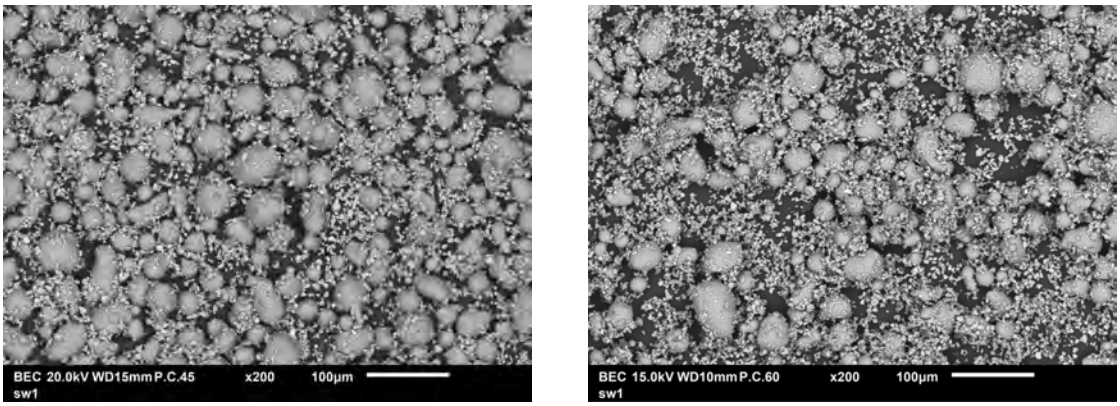

(a) (b)

Figure 3. SEM of mechanically mixed powder AlSi10Mg powder (LPW) and TiB_2 powder (U.S. Research Nanomaterials). (a) w=16 %. (b) w=30 %.

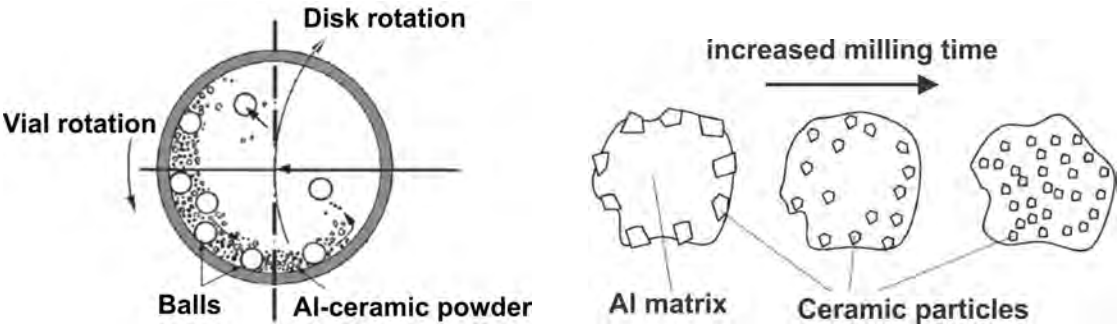

(a) (b)

Figure 4. Schematic of process to form composite particles by mechanical alloying (ball milling). (a) Impacts between the balls and between balls and the vial cause plastic deformation, cold welding, and fracture of the aluminum particles. (b) As the milling time increases, the ceramic particles decrease in size and become evenly distributed within the aluminum particles.

TABLE 3

Mechanical Alloying Parameters

Parameter	**Property**	**Value**
Disc wheel	Effective radius, r_d	90 mm
Vial:disc velocity, $\omega_\mathrm{v} : \omega_\mathrm{d}$		-2:1
Milling vials	Volume	500 mL
	Material	440C stainless steel
	Radius, r_v	45 mm
	Height, h_v	84.6 mm
Balls	Material	440C stainless steel
	Total mass	1100, 1200 g
Powder	Total mass, m_p	110–120 g
	TiB_2	10–30 wt%
Process control agent	Stearic acid	2 wt%

the milling time required. The process variables held approximately constant are summarized in Table 3.

Additional critical alloying parameters are the selection of process control agent (PCA), if any, and its mass fraction. Nearly always used in the mechanical alloying of aluminum, PCAs are organic compounds that adsorb on the surface of the particles, reducing their surface energy and therefore decreasing the driving force for cold welding. Because initial experiments without PCA showed excessive cold welding and no evidence of fracture, we chose to use a PCA for this process.

After milling, the ball mill jars were emptied under argon, and the powders were sieved and characterized. The powders were sized to 25–63 μm or 20–63μm using a sieve shaker (Fritsch ANALYSETTE 3 PRO), 8-inch sieves (Retsch or Advantech), and a batch size of 20 g per sieve set. After sieving, the powder morphology was characterized with SEM and a Malvern Morphologi G3 particle analyzer.

While experimenting with many different process parameters, we determined a range of parameters that produce composite particles with the desired properties. With 440C balls, these parameters are mill speeds of 350–450 rpm, ratio of ball mass to powder mass (BPR) of 10, vial fill ratio of about 0.55, ball diameter of 10–15 mm, and a PCA mass fraction of 2 wt%. In the alloying trials described here, 110–120 g of mixed AlSi10Mg + TiB_2 powder was added to each vial,

together with 2 wt% PCA. Depending on the mill speed, the mill was run for periods of 2 min, followed by rest periods of 10–28 min. The rest periods were designed to prevent excessive increases in temperature that would suppress the yield strength of the aluminum below the stress required to cause fracture. During rest periods, we sampled the powder at regular intervals for examination by optical microscopy, SEM, and statistical analysis.

2.2.2 Modeling of Mechanical Alloying Process

For the purpose of optimizing the production of composite powders by mechanical alloying, we adopted from the literature an analytic model describing the kinematics of planetary ball milling. This model helps to identify the process variables that significantly affect the morphology and microstructure of the powders. The following equations are based on the derivations and computations of Burgio et al. (1991), Abdellaoui and Gaffet (1995), and Murty et al. (1995).

The model describes the kinematics of a single ball in a planetary ball mill, with consideration also of the energy dissipated by impacts between balls. For a single ball, the speed at impact with the wall of the vial is

$$v_{\mathrm{b}} = \sqrt{(r_{\mathrm{d}}\,\omega_{\mathrm{d}})^2 + (r_{\mathrm{v}} - r_{\mathrm{b}})^2\,\omega_{\mathrm{v}}{}^2\left(1 - 2\frac{\omega_{\mathrm{v}}}{\omega_{\mathrm{d}}}\right)}, \tag{1}$$

where r_{b} is the radius of the ball and the other variables are defined in Table 3. The impact energy is then simply

$$E_{\mathrm{b}} = \frac{1}{2} m_{\mathrm{b}}\, v_{\mathrm{b}}^2. \tag{2}$$

The frequency of impacts is approximated as

$$f_{\mathrm{b}} \approx K\,\frac{(\omega_{\mathrm{d}} - \omega_{\mathrm{v}})}{2\,\pi}, \tag{3}$$

with $K \approx 1$, based on the time required for the ball to detach from the wall and travel across the vial. From the preceding two equations, the power of a single ball impact, or shock power, is calculated as

$$P_{\mathrm{b}} = f_{\mathrm{b}}\, E_{\mathrm{b}}. \tag{4}$$

Finally, the normalized energy input is calculated by considering the number of balls in the vial, n_{b}, the time of milling, and the mass of the powder:

$$E_{\mathrm{n}} = \frac{P_{\mathrm{b}}\, n_{\mathrm{b}}\, t}{m_{\mathrm{p}}}\,\delta, \tag{5}$$

where δ, the filling parameter, is a number between 0 and 1 that describes the decrease in milling efficiency caused by interaction between the balls. The filling parameter is phenomenologically calculated as

$$\delta = (1 - n_{\delta}^{\epsilon})\,, \tag{6}$$

TABLE 4

Mechanical Alloying Kinematic Process Variables

Ball diam. d_b (mm)	Mill speed (rpm)	Time, t (min)	v_b (m/s)	Impact E, E_b (J/hit)	Shock power, P_b (W)	Normalized E, E_n (W h/g)
9.525–14.29	350, 450	240	7.03, 9.48	0.157, 0.290	3.52, 5.08	23.1–26.0
9.525–14.29	350, 450	480	7.03–9.48	0.157–0.480	3.52–10.80	47.6–52.0

where n_δ approximates the fill ratio of the vial based on the number of balls in the vial and the number of balls that would fill the vial with simple cubic packing, n_full:

$$n_\delta \equiv \frac{n_\mathrm{b}}{n_\mathrm{full}}. \tag{7}$$

The parameter ϵ accounts for the fact that the balls do not interfere with each other until they cover about one third of the surface of the vial. For $d_\mathrm{b} = 10.3\,\mathrm{mm}$, $\epsilon = 1.497$, and for $d_\mathrm{b} = 20.0\,\mathrm{mm}$, $\epsilon = 2.041$.

This model was used to characterize and analyze several of the successful mechanical alloying experiments (Table 4). The results of previous investigators indicate that it is the normalized total energy input, E_n, that primarily governs the end product. However, in some cases, it was shown also that this energy must be supplied at a minimum impact energy or shock power. The results indicate that a normalized total energy input of $E_\mathrm{n} \gtrsim 70\,\mathrm{W\,h/g}$ is sufficient to form particles with the desired morphology. Furthermore, the results show that impact energy $E_\mathrm{b} \geq 0.15\,\mathrm{J}$ and shock power $P_\mathrm{b} \geq 11\,\mathrm{W}$ are adequate.

2.2.3 Morphology of Mechanically Alloyed Composite Powders

The successful alloying trials exhibited trends that are characteristic of the mechanical alloying of most ductile metals. Figure 5 shows a typical result with 10 mm balls, starting with a mix of LPW Standard aluminum powder and U.S. Nano TiB_2 powder. Initially, the ductile aluminum particles plastically deform and weld to each other, forming large plate-like particles (Figure 5 b,c). Then, between 120 min and 180 min of milling, the aluminum strain hardens to an extent that brittle fracture can occur, and the particles begin to decrease in size and become more spherical (Figure 5 d,e). After 240 min of milling, corresponding to a normalized energy input of E_n=26.1 Wh/g, the alloyed particles are similar in size to the starting aluminum powder and reasonably equiaxed. At this time, welding and fracture are approaching a state of equilibrium with each other.

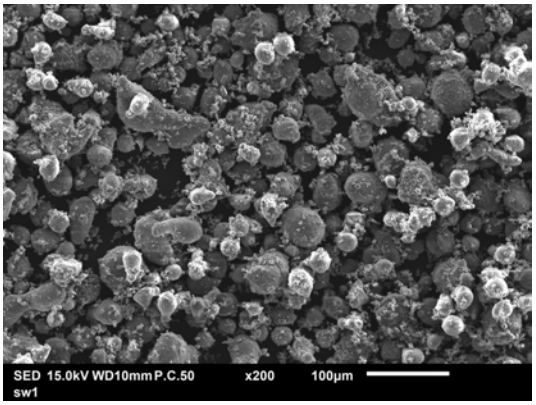

(a)

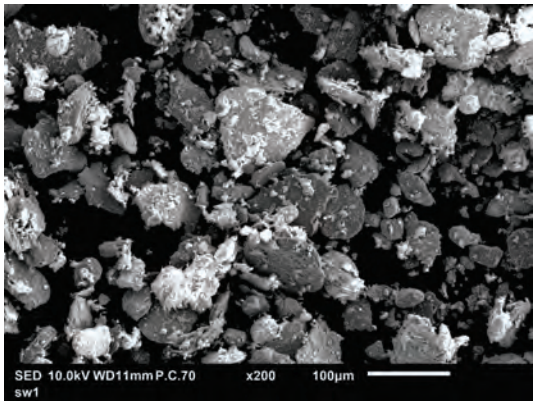

(b)

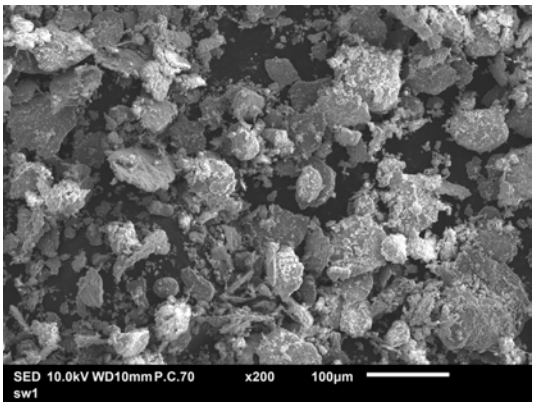

(c)

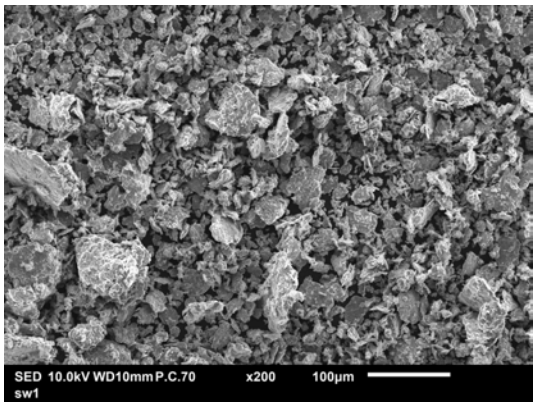

(d)

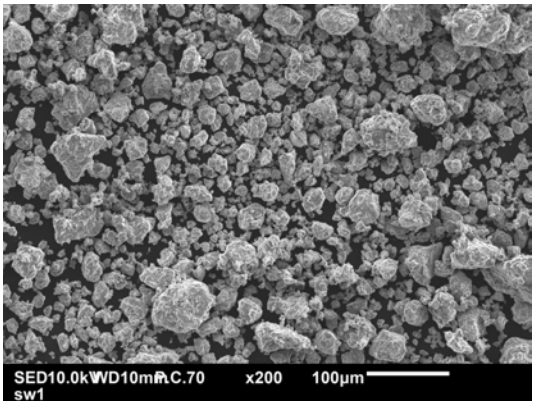

(e)

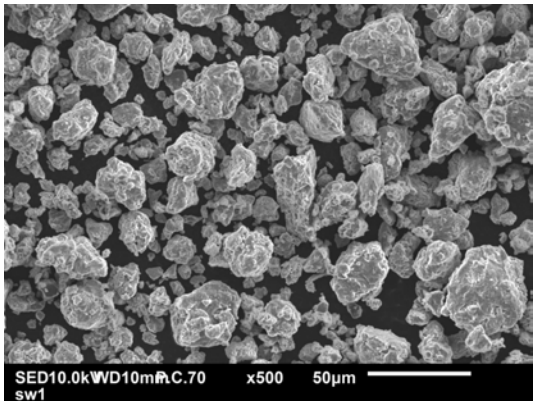

(f)

Figure 5. High speed ball milling of LPW AlSi10Mg standard powder with U.S. Nano TiB_2 powder at 10 wt% ceramic. (a) Starting blend. (b) t=60 min, E_n=6.5 Wh/g. (c) t=120 min, E_n=13.0 Wh/g. (d) t=180 min, E_n=19.5 Wh/g. (e) t=240 min, E_n=26.1 Wh/g. (f) t=240 min at high magnification. (Mill speed=450 rpm, $d_b = 10.3$ mm, BPR=10, PCA: stearic acid at 2 wt%.)

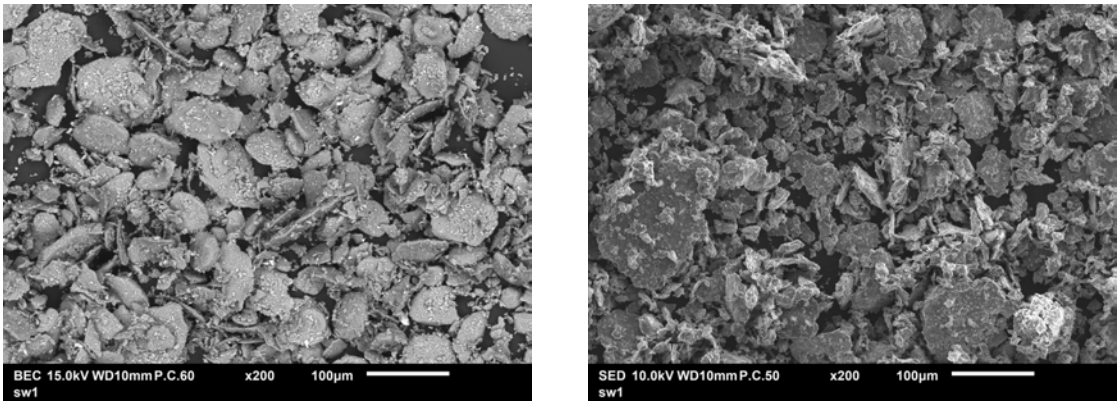

(a) (b)

Figure 6. Moderate speed ball milling of LPW AlSi10Mg standard powder with U.S. Nano TiB_2 powder at 10 wt% ceramic. (a) t=240 min with ball diameter d_b=10.3 mm, E_n=18.7 Wh/g. (b) t=240 min with ball diameter d_b=20 mm, E_n=17.8 Wh/g. (Mill speed=320 rpm, BPR=10, PCA: stearic acid at 2 wt%.)

Decreasing the mill speed to 320 rpm decreases both the energy per impact and the frequency of impacts. As a result, after 240 min of milling, the particles are still large and flat (Figure 6). At this speed, additional milling time is required for fracture to occur, assuming that the impact energy is adequate to cause fracture eventually. The advantage to milling at low speed is that the temperature rise of the material will be lower than it is at high speed, potentially causing welding and fracture to equilibrate at a smaller particle size.

Quantitative particle analyses conducted with a Malvern Morphologi G3 confirm the SEM observations and characterize the effects of ball size and mill speed (Figure 7). At short milling times, when plastic deformation and cold welding are dominant, the average particle diameter by volume, d_{50}, increases. After longer periods of milling, fracture becomes prevalent and the particle size decreases. The trend in number of particles per sample is less clear, but generally the number of particles decreases with increasing milling time, as fracture competes with both cold welding of the aluminum and alloying of the two phases (i.e., the ceramic particles are consumed by the aluminum). At a fixed mill speed of 450 rpm, increasing the diameter of the balls from 10.3 mm to 20 mm does not significantly affect the results at $t = 120$ min. However, the particles temporarily grow larger than they do with 10.3 mm balls due presumably to the increase in temperature that accompanies the large increase in energy per impact ($E_b \propto d^3$).

These initial results confirmed our understanding of the ball milling process and verified that this method could indeed be used to manufacture composite powders for SLM. We then explored the effects on particle morphology of initial ceramic content, impact energy, and normalized energy input. The goal of this study was to maximize both the performance and the yield of the powder.

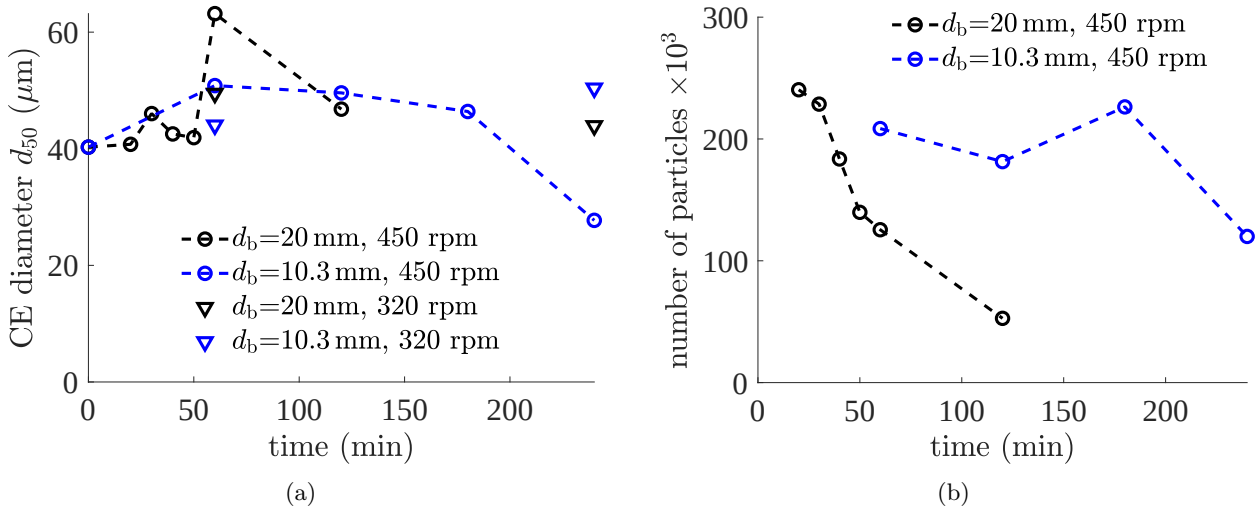

Figure 7. Effect of ball size, mill speed, and milling time on morphology of composite particles. (a) Particle diameter. (b) Number of particles per 5 mm^3 sample. (w=10%.)

The results show that the morphology of the ball-milled powders is a strong function of both the ceramic content and the normalized energy input (Figures 8–13). At $w = 0$ and $E_n \approx 50\,\mathrm{W\,h/g}$, the powder is plate-like and exhibits many flat surfaces because the powder has apparently not hardened sufficiently to prevent yield and initiate fracture (Figures 8 and 9a). It is not until energies exceeding $E_n \approx 150\,\mathrm{W\,h/g}$ that the plain AlSi10Mg powder exhibits the nearly equiaxed, spherical shape that we desire (Figures 8b and 9b). However, adding the ceramic particles accelerates the milling process, and, at $w = 16\%$, an energy input of only $E_n \approx 24.1\,\mathrm{W\,h/g}$ is sufficient to produce a powder with suitable morphology (Figures 10a and 11a). The ceramic particles apparently cause concentrations of stress within the aluminum particles that increase the rate of strain hardening. Approximately doubling the energy input to $E_n = 51.9\,\mathrm{W\,h/g}$ slightly improves the particle morphology by reducing the aspect ratio and surface roughness of the particles (Figures 10b and 11b). The ball-milled powders with $w = 30\%$ obey this trend, exhibiting excellent, spherical morphology at only $E_n = 26.0\,\mathrm{W\,h/g}$ (Figures 12a and 13a). In this case, increasing the energy input to $E_n \approx 150\,\mathrm{W\,h/g}$ substantially reduces the surface roughness of the particles, and there are very few small satellites decorating the large particles (Figures 12b and 13b). Further increasing the energy input beyond about $E_n = 150\,\mathrm{W\,h/g}$ did not improve the powder morphology. Because higher input energies also reduced yield and increased cold welding, we focused on energies in the range of $E_n \approx 25 - 50\,\mathrm{W\,h/g}$

Particle analysis confirmed numerically that the sieved composite powders are similar in morphology to the original gas atomized AlSi10Mg powder. The particle size distribution (PSD)

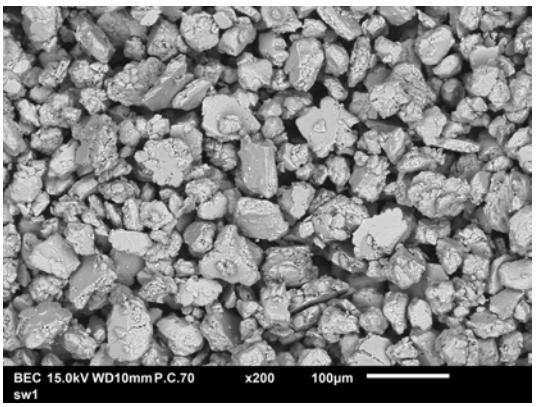

(a)

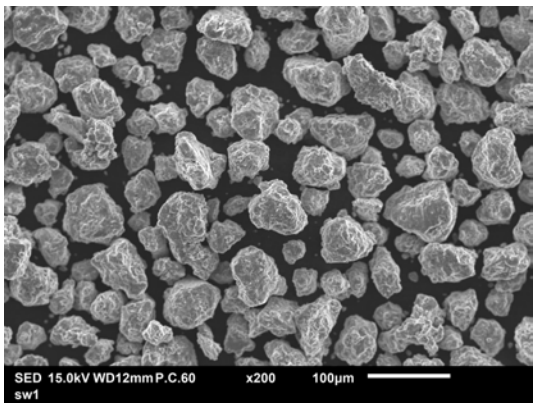

(b)

Figure 8. SEM of ball-milled powders, plain AlSi10Mg, sieved 20–63 µm. (a) E_n=51.9 Wh/g. (b) E_n=156.2 Wh/g.

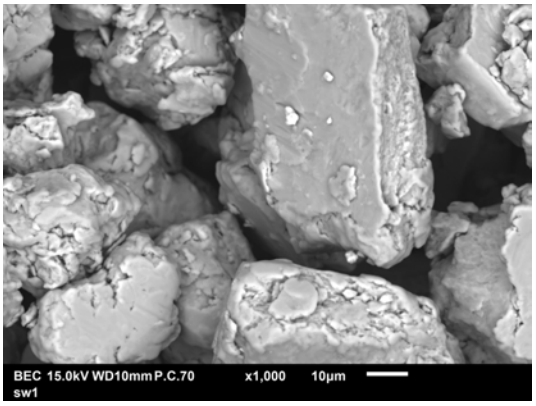

(a)

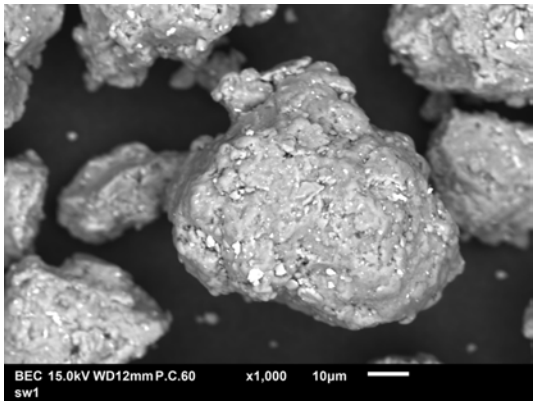

(b)

Figure 9. SEM of ball-milled powders, plain AlSi10Mg, sieved 20–63 µm. (a) E_n=51.9 Wh/g. (b) E_n=156.2 Wh/g.

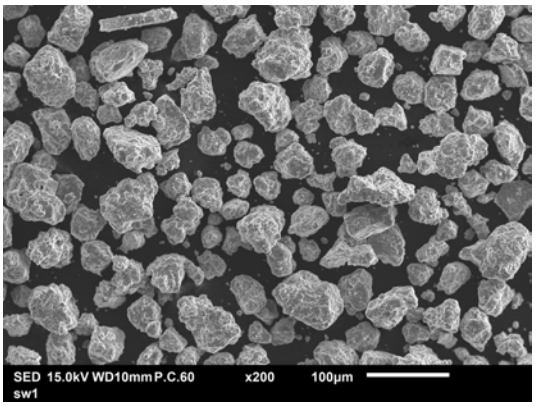

(a)

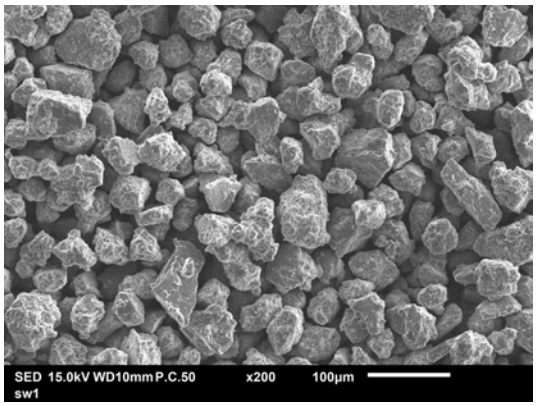

(b)

Figure 10. SEM of ball-milled powders, w=16%, sieved 25–63 µm. (a) E_n=24.1 W h/g. (b) E_n=51.9 W h/g.

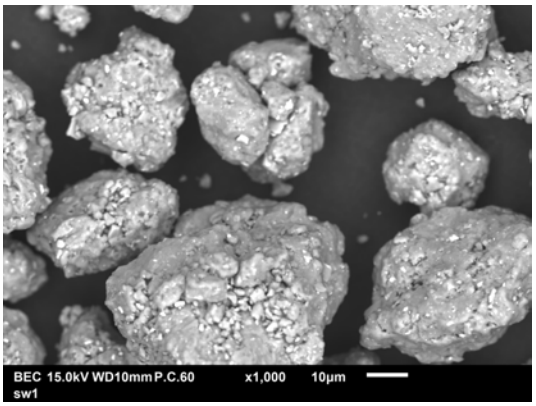

(a)

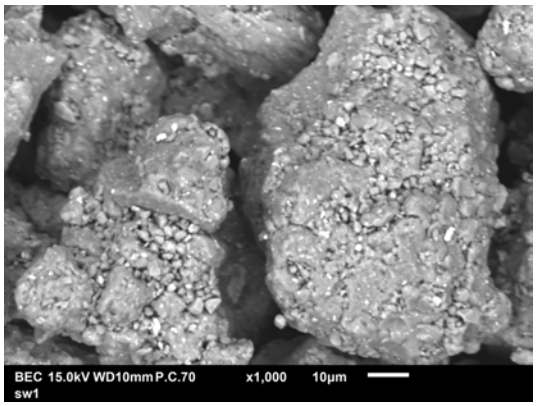

(b)

Figure 11. SEM of ball-milled powders, w=16%, sieved 25–63 µm. (a) E_n=24.1 W h/g. (b) E_n=51.9 W h/g.

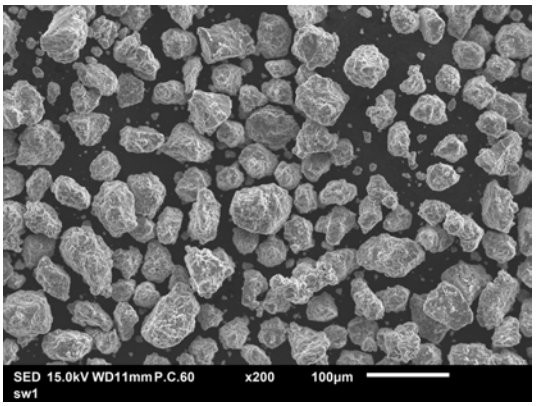

(a)

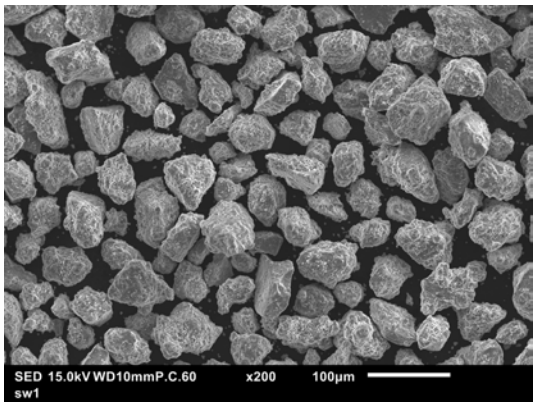

(b)

Figure 12. SEM of ball-milled powders, w=30%, sieved 25–63 µm. (a) E_n=26.0 W h/g. (b) E_n=52.0 W h/g.

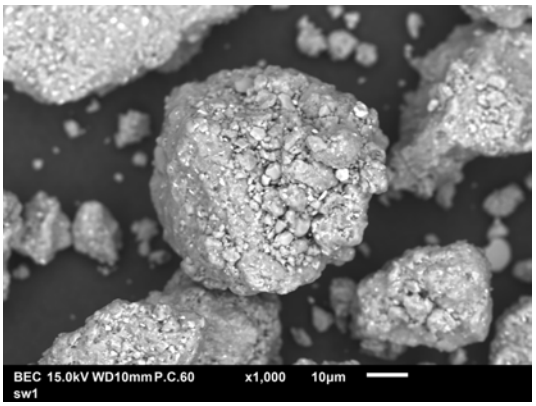

(a)

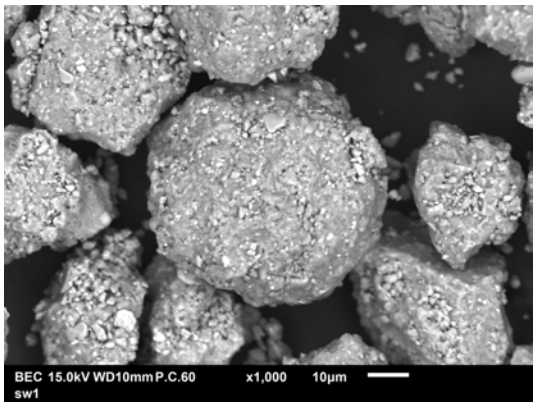

(b)

Figure 13. SEM of ball-milled powders, w=30%, sieved 25–63 µm. (a) E_n=26.0 W h/g. (b) E_n=52.0 W h/g.

of the gas atomized powder exhibits a single smooth peak at a diameter of $d \approx 41\,\mu m$ (Figure 14a), which packs and flows reasonably well (for a light material such as aluminum). However, when the ceramic particles are mixed in, the PSD becomes bimodal (Figure 14b), and the powder no longer flows well because the small ceramic particles interfere with the rolling of the aluminum particles, jamming up the flow. Therefore, our goal was to produce a composite powder with a single PSD peak so that the powder could be reliably spread in the thin, uniform layers required by the SLM process. The PSDs for the composite powders closely resemble the PSD of the gas atomized powder, providing further evidence the composite powders will perform well in the SLM machine (Figure 14 c–f). Summarized in Table 5, the ranges of particle size (d10 − d90) are all within $20 - 76\mu$m, and the sieved yield percentage varies from 30% up to over 50%.

By qualitative measures, the composite powders fabricated by mechanical alloying appear to flow much better than the original mixed powders do. They readily roll down the wall of their container at angles for which the mixed powders would remain firmly adhered to the wall. The improvement in flowability is caused primarily by the migration of the ceramic particles to the interior of the aluminum particles. While powders produced by mechanical alloying are not as spherical as gas atomized powders, they commonly have narrow size distributions, which also favors flowability. This narrow size distribution is evident in Figure 14, in which the PSDs of the composite powders are more square in shape than the PSD of the gas atomized powder.

The efficacy of the ball milling was characterized further with XRD scans that measured the structural changes in the powder as a function of ceramic content and energy input. A Rigaku SmartLab diffractometer was used with a monochromatic Cu Kα radiation source ($\lambda = 0.15406\,$nm) operating at 30 mA and 40 kV. Symmetric Bragg-Brentano θ-2θ scans were collected over a range of $2\theta = 10 - 145^\circ$ with a step size of $\Delta\theta = 0.005^\circ$ and a count time of 1 s. A 1-D scanning detector mode was used in order to maximize the scan resolution. The average crystallite size of the milled powders was calculated from the broadening of the first four aluminum reflections using a modified Scherrer equation and the Williamson-Hall plot method (full width at half maximum). In addition, for the milled composite powders, a quantitative analysis was conducted using the Whole Pattern Fitting method with Rietveld refinement to fit the diffraction patterns to experimental data in the ICDD PDF-4+ database.

In both the gas atomized and the milled AlSi10Mg powders, aluminum and silicon X-ray peaks were identified (Figure 15). As the milling energy increases, these peaks decrease in height and increase in width at half peak, indicating that the crystallite size is decreasing. The decrease in grain size is attributed to the formation of localized shear bands with a high density of dislocations. When the strain becomes large enough, these dislocations annihilate and small angle grain boundaries form in their place (Lu and Lai, 1998). An energy input of $E_\mathrm{n} = 51.9\,$Wh/g causes the crystallite size to decrease from 81.7 nm to 32.0 nm (Table reftab:XRD). Additional milling to $E_\mathrm{n} = 156.2\,$Wh/g causes a further refinement to only 30.4 nm, suggesting that the process has reached a state of equilibrium.

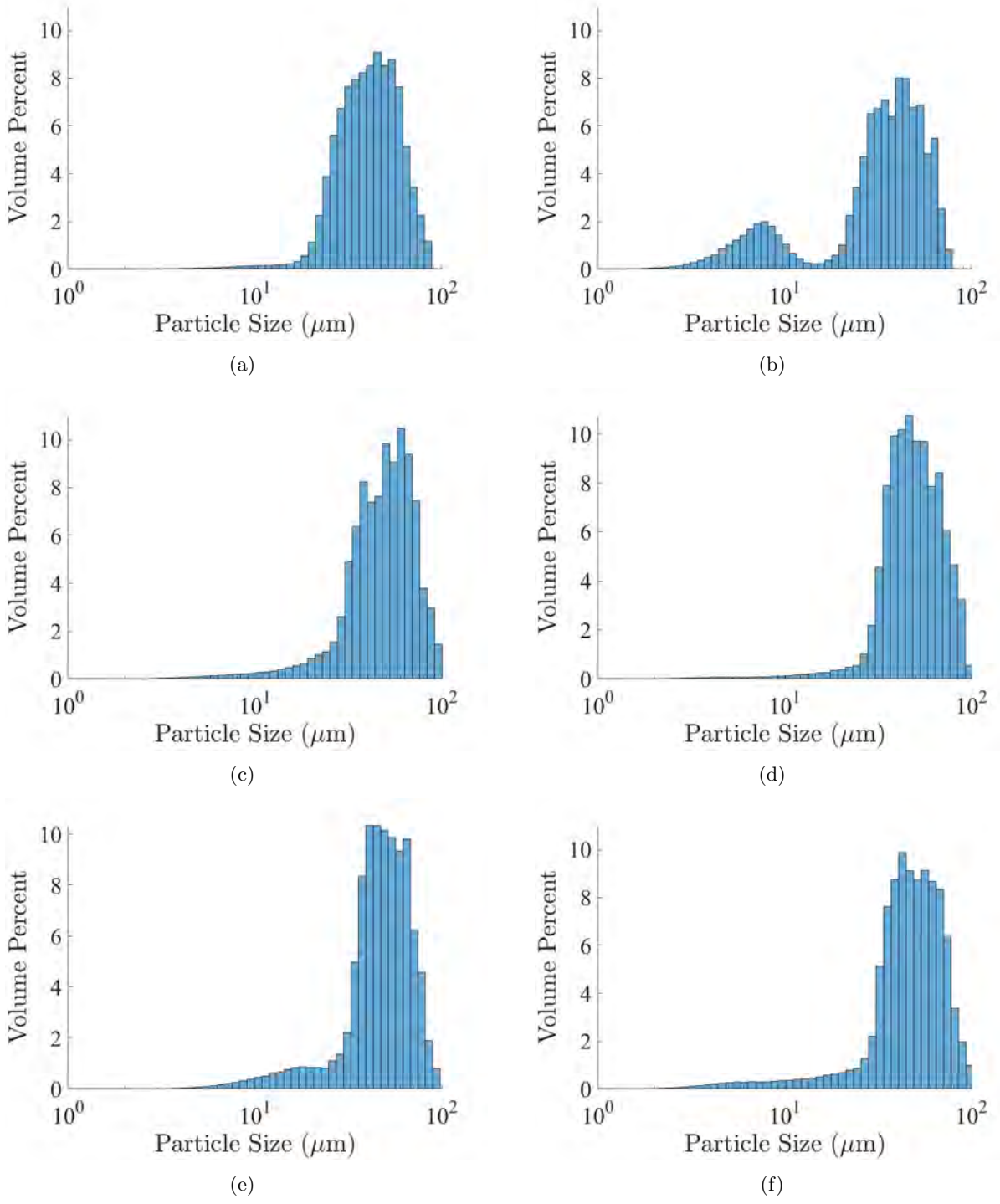

Figure 14. Particle size analysis of powders. (a) Gas atomized AlSi10Mg. (b) Mixed AlSi10Mg + 16 wt% TiB_2. (c) Mechanically alloyed AlSi10Mg + 16 wt% TiB_2, E_n=26.0 W h/g. (d) Mechanically alloyed AlSi10Mg + 16 wt% TiB_2, E_n=47.6 W h/g. (e) Mechanically alloyed AlSi10Mg + 30 wt% TiB_2, E_n=26.0 W h/g. (f) Mechanically alloyed AlSi10Mg + 30 wt% TiB_2, E_n=52.0 W h/g.

TABLE 5

Properties of Mechanically Alloyed Powders

Initial TiB_2 wt%	Milling energy, E_n (W h/g)	Impact energy (J/hit)	Yield 20–63 μm	Yield 25–63 μm	Particle sizes (μm) d10	d50	d90
0 (LPW-R2)	51.9	0.157	51.63%	-	29.9*	45.1*	69.4*
0 (LPW-R3)	156.2	0.157	49.55%	43.33%	35.2	49.7	73.2
16% (R13)	24.1	0.157	53.65%	38.07%	28.8	47.9	75.1
16% (R10)	47.6	0.157	-	27.30%	32.4	46.3	71.0
16% (R14)	51.9	0.157	51.37%	32.37%	32.7	49.2	74.3
20% (R17)	24.5	0.290	40.10%	-	24.6*	43.9*	71.4*
20% (R18)	24.9	0.290	43.78%	-	24.7*	48.1*	75.6*
20% (R16)	52.0	0.480	57.35%	39.33%	20.3	45.1	73.2
30% (R12)	26.0	0.157	-	30.01%	27.2	48.7	71.7
30% (R15)	52.0	0.180	57.44%	32.20%	27.5	47.0	74.0

*Sieved $20 - 63\,\mu$m

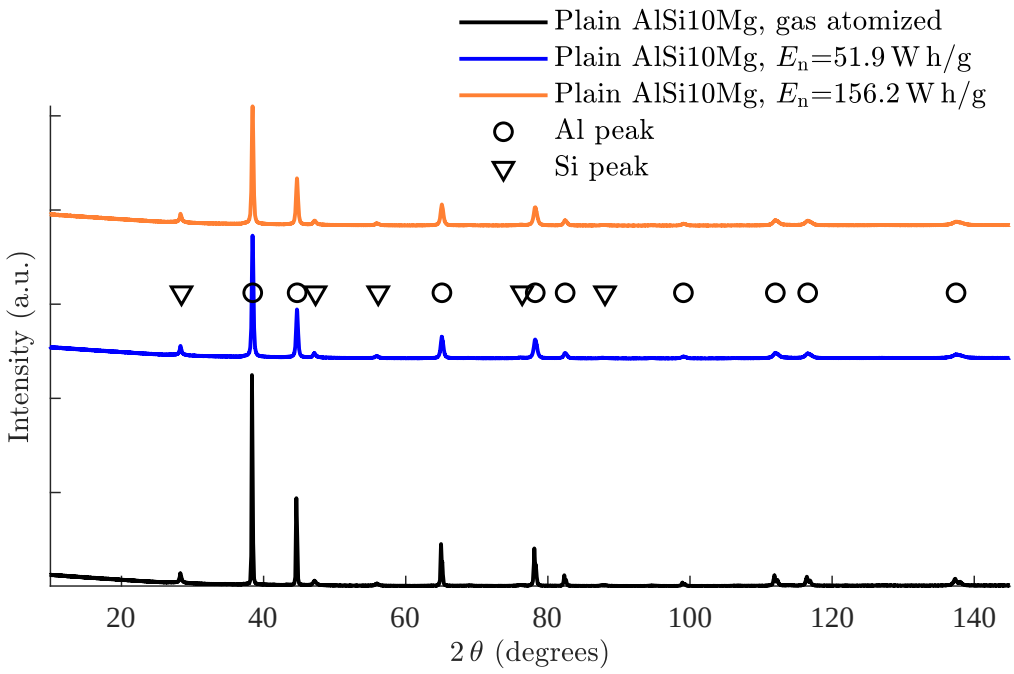

Figure 15. XRD scans of gas atomized AlSi10Mg and ball-milled AlSi10Mg.

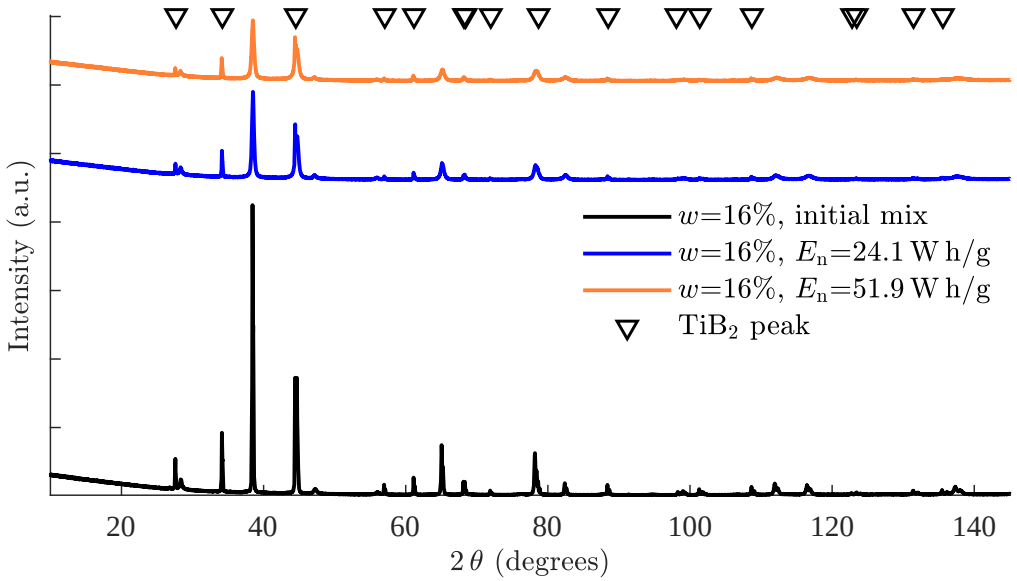

Figure 16. XRD scans of initial mix and ball-milled powders at w=16%.

Characterization of the mixed and milled composite powders at $w = 16\%$ and $w = 30\%$ identified also the TiB_2 phase and revealed further refinement of the microstructure of the powders (Figures 16 and 17). Furthermore, there are no unidentified phases, indicating that reactions producing intermetallics did not occur during milling. The weight fractions of TiB_2 in the milled powders are $16.3 - 17.2\%$ and $28.9 - 31.1\%$, nearly identical to the proportions in the initial mixes, providing quantitative evidence that we have successfully reinforced the aluminum particles. Similar to the plain AlSi10Mg powders, the crystallite size decreases as the milling energy increases, but the rate of refinement increases with increasing weight fraction of ceramic. At $w = 30\%$, an energy input of only $E_n = 26.0\,\mathrm{Wh/g}$ is sufficient to reduce the crystallite size to 19.5 nm. Approximately doubling the energy input to $E_n = 52.0\,\mathrm{Wh/g}$ causes only a small reduction in crystallite size to 18.1 nm, indicating that the microstructure has stabilized and additional milling will not cause significant changes. The more rapid evolution of the microstructure with increasing ceramic content is presumably related to the plastic work associated with the stress concentrations generated by the small, hard ceramic particles. This theory is supported by the observation that jars containing composite powders increase in temperature more quickly than jars containing unmodified powder. Finally, we note that the intensity of the TiB_2 peaks also decreases with increasing input energy (Figures 16 and 17. This trend suggests that we have also been successful in reducing the size of the ceramic particles.

Sectioning of the ball-milled powders confirmed that alloying of the AlSi10Mg and TiB_2 was successful (Figures 18–21). The SEM images demonstrate that each alloyed particle consists of an

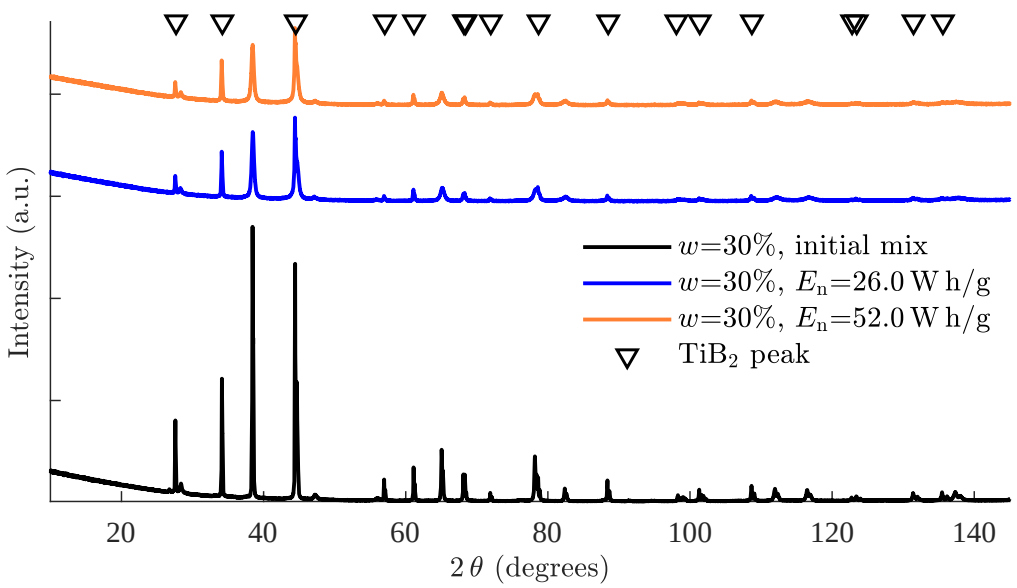

Figure 17. XRD scans of initial mix and ball-milled powders at w=30%.

TABLE 6

XRD Characterization of Plain Aluminum and Composite powders

Initial TiB_2 wt%	Milling energy, E_n (W h/g)	Al crystallite size (nm)	Al wt%	TiB_2 wt%	Si wt%
0	0 (GA)	81.7 ± 12.7	89.5	0	9.9
0	51.9	32.0 ± 7.0	89.2	0	10.2
0	156.2	30.4 ± 6.9	89.2	0	10.1
16% (R13)	24.1	25.6 ± 4.7	77.0	16.3	6.7
16% (R10)	47.6	19.0 ± 4.0	76.2	17.2	6.6
16% (R14)	51.9	19.2 ± 4.2	75.4	17.2	7.4
30% (R12)	26.0	19.5 ± 4.3	64.9	28.9	6.1
30% (R15)	52.0	18.1 ± 4.3	63.5	31.1	5.5

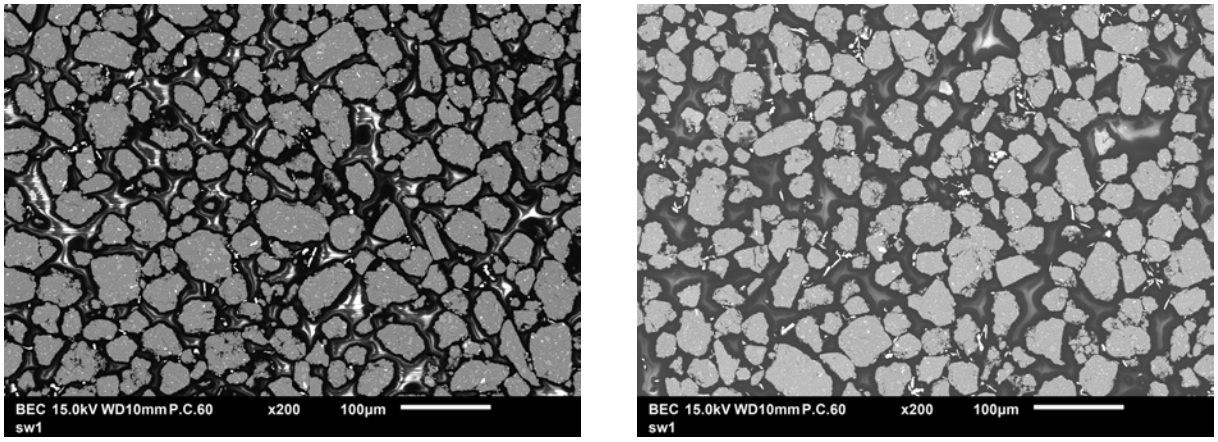

(a) (b)

Figure 18. Sectioned AlSi10Mg + 16 wt% TiB_2 particles after mechanical alloying, sieved 25–63 µm. (a) E_n=24.1 Wh/g. (b) E_n=51.9 Wh/g.

AlSi10Mg matrix uniformly modified with micron-sized TiB_2 particles. (In backscatter mode, the TiB_2 particles appear lighter in color than the aluminum does.) Powder with this morphology should flow well and ensure distribution and wetting of the ceramic within the molten aluminum. Phase analysis by EDS confirms that these particles are indeed composed of TiB_2.

The SEM and EDS images also reveal two important, positive trends in particle morphology. At both weight fractions, with increasing energy input, both the ceramic particle size and the volume fraction of internal porosity decrease. At $E_n \approx 150\,\mathrm{W\,h/g}$, the TiB_2 particle size has decreased from $d = 2 - 12\,\mu\mathrm{m}$ to $d \lesssim 2\,\mu\mathrm{m}$ and there is negligible internal porosity. (Even gas atomized SLM powders contain internal pores.)

2.2.4 Performance of Mechanically Alloyed Composite Powders

In SLM, the quality of the powder bed is determined to a large extent by the properties of the powder itself. (The method of spreading, or recoating, also plays a role.) For a given particle shape, broadening the distribution of particle sizes increases the theoretical packing density, but, even with a distribution of sizes, powder beds with packing densities greater than 0.6 are rarely attained. The property that limits packing density is the ease with which the powder flows, or flowability, when it is spread over the build plane by the recoater blade or roller. Flowability is maximum with monodisperse, spherical particles and decreases with decreasing particle size. As the particle size decreases, the specific surface area of the powder increases, and the magnitude of adhesive and cohesive forces, including van der Waals and electrostatic forces, increases relative to the magnitude of the forces due to gravity, inertia, and contact with the recoater. While increasing

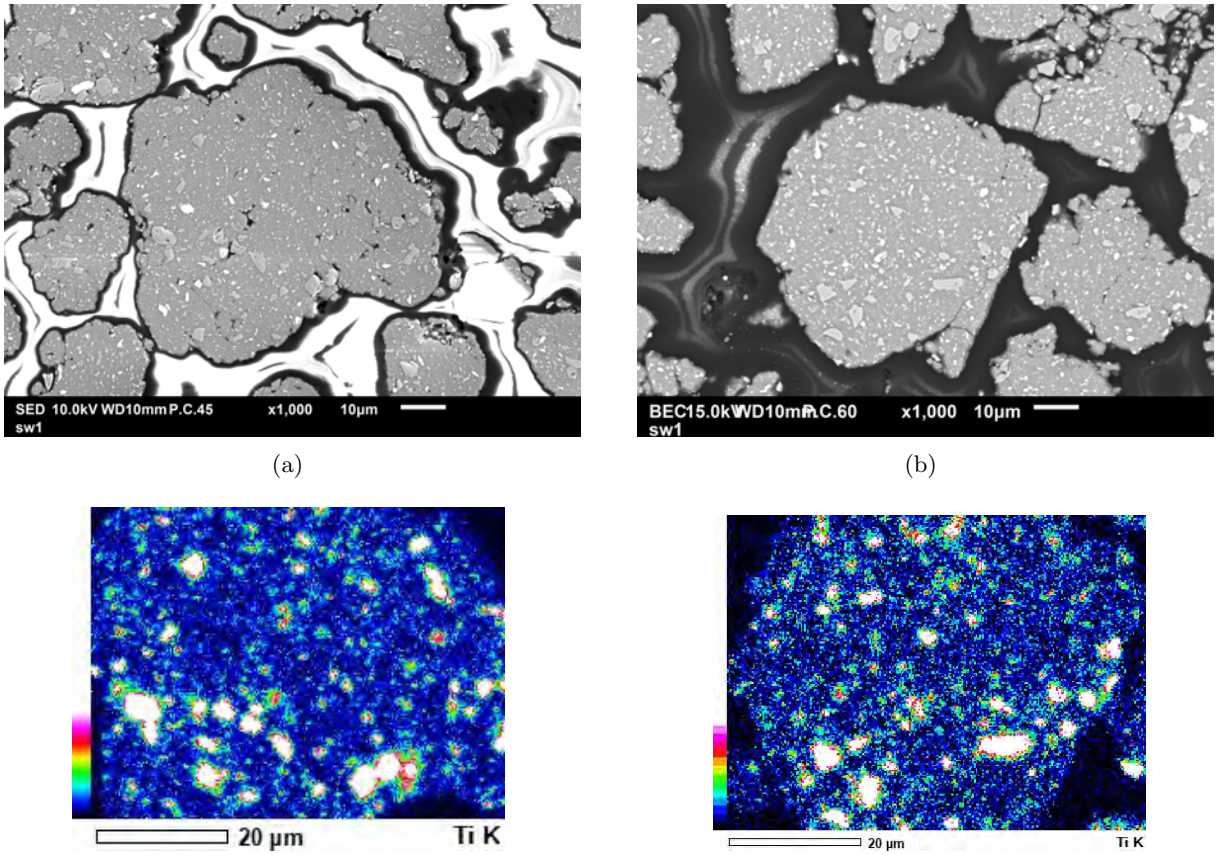

(a) (b)

(c) (d)

Figure 19. Sectioned AlSi10Mg + 16 wt% TiB_2 particles after mechanical alloying, sieved 25–63 µm. (a) SEM at E_n=24.1 Wh/g. (b) SEM at E_n=47.6 Wh/g. (c) EDS at E_n=24.1 Wh/g. (d) EDS at E_n=47.6 Wh/g.

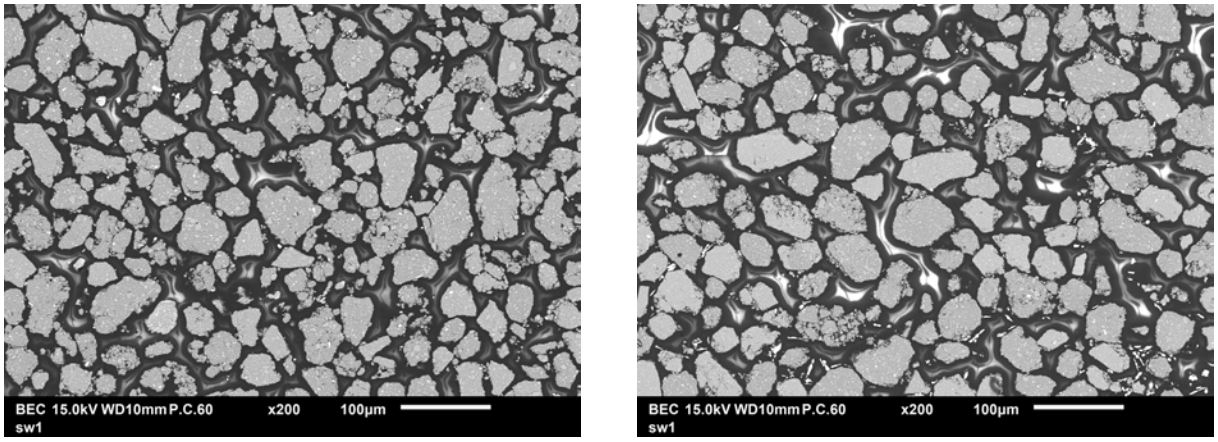

(a) (b)

Figure 20. Sectioned AlSi10Mg + 30 wt% TiB_2 particles after mechanical alloying, sieved 25–63 µm. (a) E_n=26.0 Wh/g. (b) E_n=52.0 Wh/g.

the dispersion of the particle size can increase packing density, it also reduces flowability because the area of particle contacts increases and small particles interfere with the rolling of large particles.

The flow and packing performance of the gas atomized, mixed, and milled powders were characterized by two simple, benchtop tests. The flow performance was measured with the Hall flowmeter. Intended for free flowing powders, the Hall flowmeter consists of a funnel with a 30° internal cone angle and an orifice diameter of 2.5 mm. In the test, the time for 50 g of powder to flow through the funnel is recorded. The packing performance was characterized by measuring the apparent density of the powders with an Arnold meter. In this test, a brass bushing is partially filled with powder and slid across a 20 cm^3 through-hole in a precision machined steel block. The block is placed over a sheet of weighing paper, and, after the hole is filled, the block is removed and the powder is weighed, providing the apparent density, ρ_{app}, of the 20 cm^3 sample. From the apparent density, the relative density can be calculated:

$$\rho_{rel} \equiv \frac{\rho_{app}}{\rho_{sol}}$$

Admittedly, these tests cannot precisely predict how the powder will perform in the actual SLM machine because they do not characterize the powder under the conditions of shear flow that the recoater imposes. However, the results of these tests do serve as valuable indicators of the flow and packing characteristics during recoating.

Because the ball milling was performed under argon, the powder was removed from the jars and tested in an argon-filled glovebox to preserve its original, as-milled condition. In these tests,

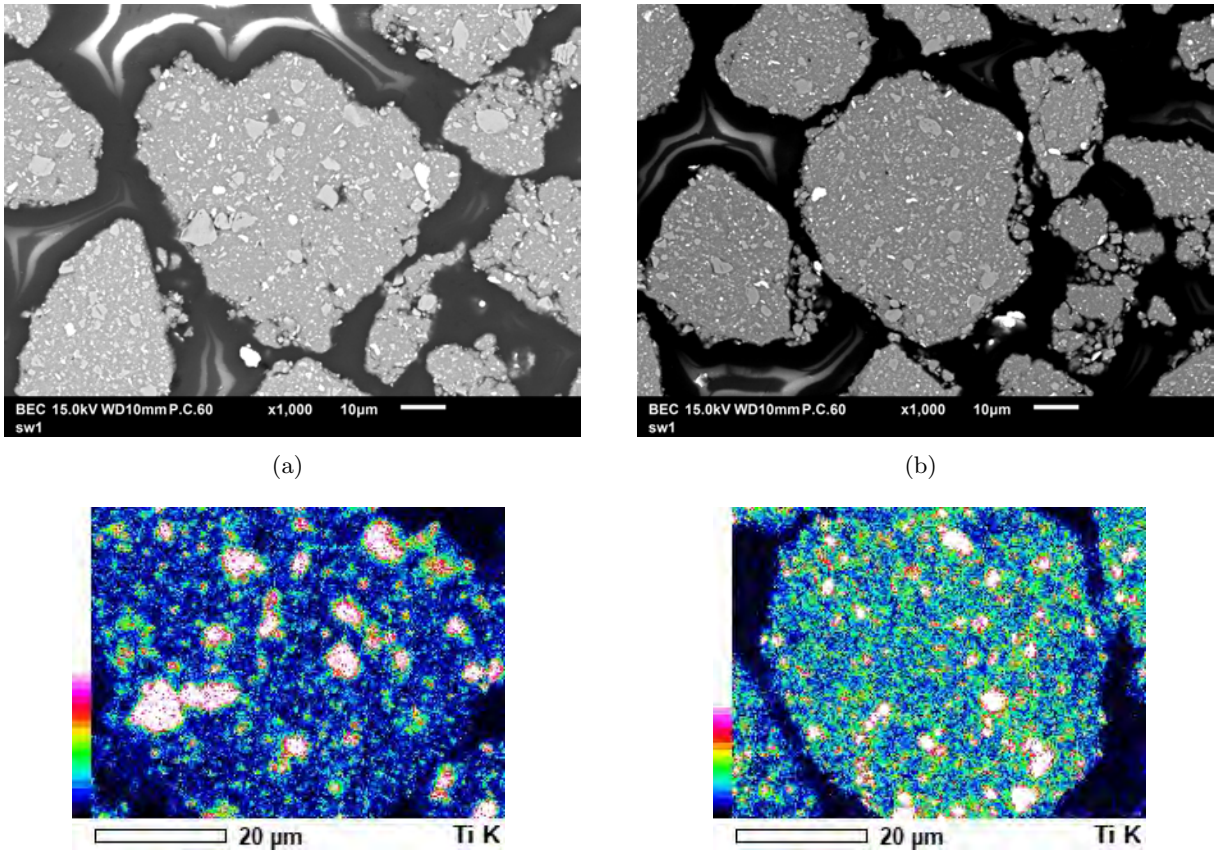

(a) (b)

(c) (d)

Figure 21. Sectioned AlSi10Mg + 30 wt% TiB_2 particles after mechanical alloying, sieved 25–63 µm. (a) SEM at E_n=26.0 Wh/g. (b) SEM at E_n=52.0 Wh/g. (c) EDS at E_n=26.0 Wh/g. (d) EDS at E_n=52.0 Wh/g.

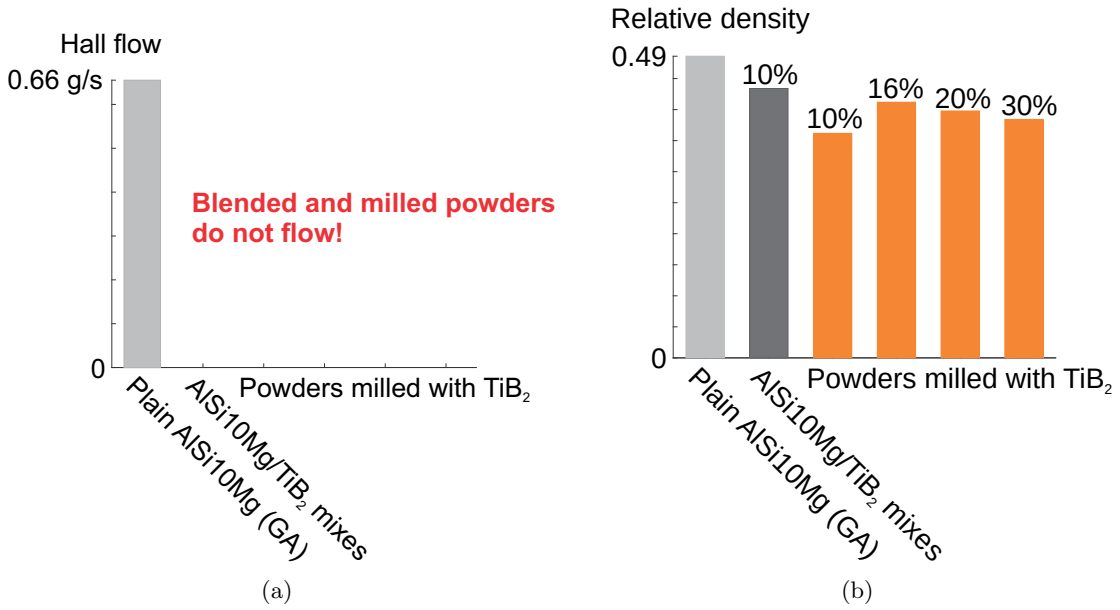

Figure 22. Performance of powders inside glovebox before passivation. (a) Hall flowability. (b) Apparent density.

the flowability and relative density of the mixed and milled powders were poor at all contents of ceramic. None of the mixed or milled powders flowed through the Hall funnel and the relative density was only about 40% in the best case (Figure 22). However, when we loaded the milled powder into the SLM machine, we noticed that it packed densely in the supply cylinder. We then retested the powders after exposure to air and found that the flowability and relative density were markedly approved. The milled powders exhibited Hall flow rates and relative densities comparable to those of the gas atomized AlSi10Mg powder and superior to the purely mixed powders (Figure 23 and Table 7).

During milling, the preexisting aluminum oxide film on the surface of the AlSi10Mg particles is broken down and distributed throughout the interior of the composite particles. Therefore, after the milling is complete but before the composite powders are reexposed to air, the particles possess clean, active surfaces with high surface energy. The high surface energy increases the interparticle cohesion and prevents the as-milled powder from flowing or packing well.

For rapid, direct evaluation of powder recoating characteristics, a simple manual test was devised. Thin plates of forged AlSi12 were milled flat and bead blasted with a 50 μm bead size to promote adhesion of powder to the plate. Next, two sections of tape, each about 75 μm thick, were applied to either side of the plate to serve as shims. We then placed small samples of powder

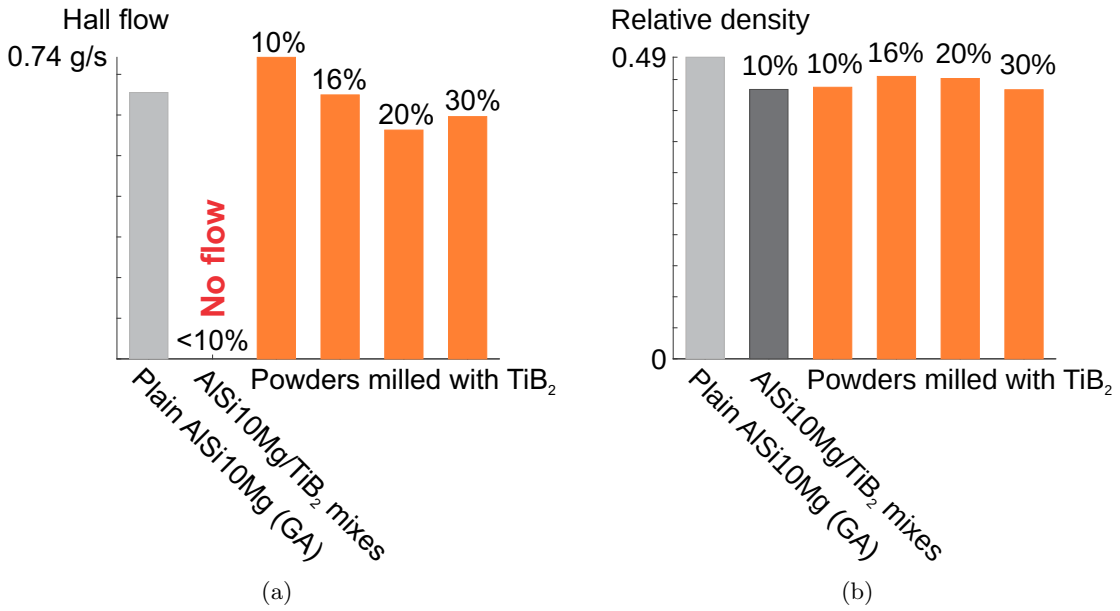

(a) (b)

Figure 23. Performance of powders after exposure to air and passivation. (a) Hall flowability. (b) Apparent density.

TABLE 7

Powder Performance

Initial TiB_2 wt%	Milling energy, E_n (W h/g)	Shock Power (J/hit)	Hall flow (s/50 g)	Apparent density, bare (g/cm^3)	Apparent density, oxid. (g/cm^3)
LPW 0% (Gas atom.)	0	-	76.3	-	1.32
16% (Init. mix)	0	-	*no flow*	-	1.31
30% (Init. mix)	0	-	*no flow*	-	1.27
0% (LPW-R2)	51.9	0.157	*no flow*	-	1.21
0% (LPW-R3)	156.2	0.157	115.3*, 74.0	1.11*	1.21
16% (R13)	24.1	0.157	88.7	1.22	1.32
16% (R10)	47.6	0.157	76.6	1.06	1.28
16% (R14)	51.9	0.157	65.6	1.14	1.28
20% (R17)	24.5	0.290	101.4*	1.20*	1.33*
20% (R18)	24.9	0.290	94.7*	-	1.34*
20% (R16)	52.0	0.480	88.8	1.11	1.30
30% (R12)	26.0	0.157	85.2	-	1.36
30% (R15)	52.0	0.180	82.6	-	1.33

*Sieved $20 - 63\,\mu$m

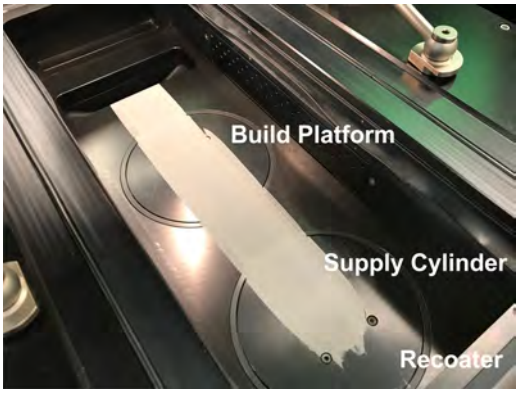

(a)

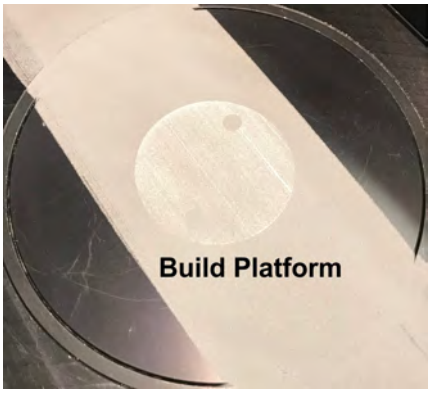

(b)

Figure 24. Composite powders with ceramic contents of up to 30% were spread in thin, uniform layers by the recoater of the SLM testbed.

at one end of the plate and attempted, by hand, to rake the powder over the plate with a beveled steel blade designed for SLM recoating. The blade successfully spread all the milled powders, but it could not spread any of the purely mixed powders in the thin, uniform layers that maximize melt pool stability and part quality during SLM.

The most relevant measures of flowability take place in an actual SLM machine or an experiment that simulates powder recoating. Despite differences in measured flow properties, all the milled composite powders could be spread by the recoater of the SLM testbed in sufficiently thin and uniform layers. On the other hand, the recoater could not spread any of the blended powders. (Figure 24–the SLM testbed is described in Section 3.1.)

2.3 SUMMARY OF MECHANICAL ALLOYING RESULTS

Here, we briefly summarize the composite powder properties in graphical format. Our conclusions are as follows:

- Flowability increases slightly with increasing input energy, presumably because the surface roughness of the particles decreases with increasing input energy (Figure 25a).
- There is not a significant correlation between relative density and input energy (Figure 25b).
- Flowability decreases weakly with increasing ceramic content, perhaps because more ceramic particles decorate and roughen the surface of the composite particles at high loadings of ceramic (Figure 26a).

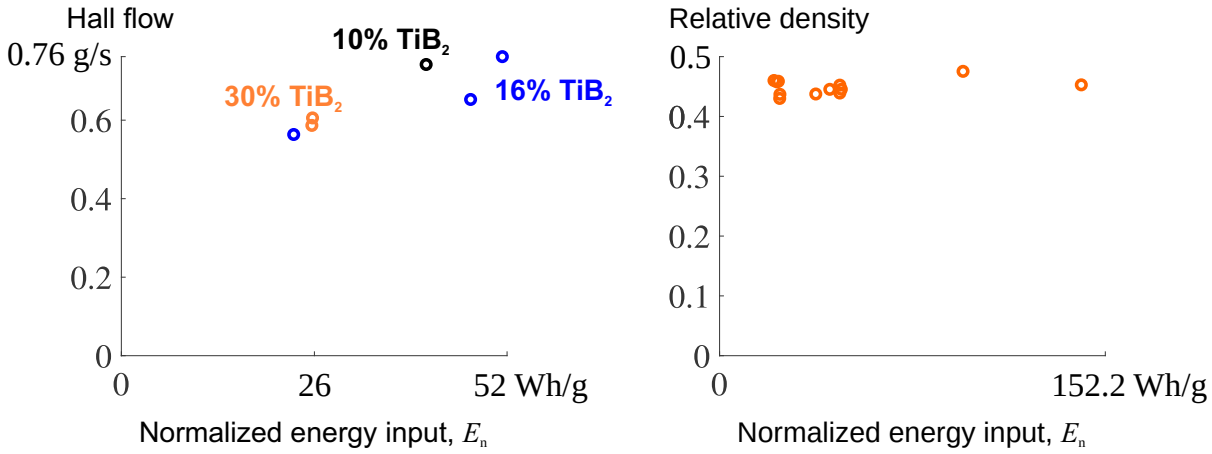

(a) (b)

Figure 25. Composite powder performance as a function of energy input.

- There is not a significant correlation between relative density and input energy (Figure 26b).
- There is not a significant correlation between powder yield and input energy (Figure 27a).
- Powder yield generally decreases with increasing ceramic content because the hard ceramic particles act as an additional grinding agent, causing fine aluminum particles to form, before the ceramic is broken down and subsumed by the aluminum particles (Figure 27b).

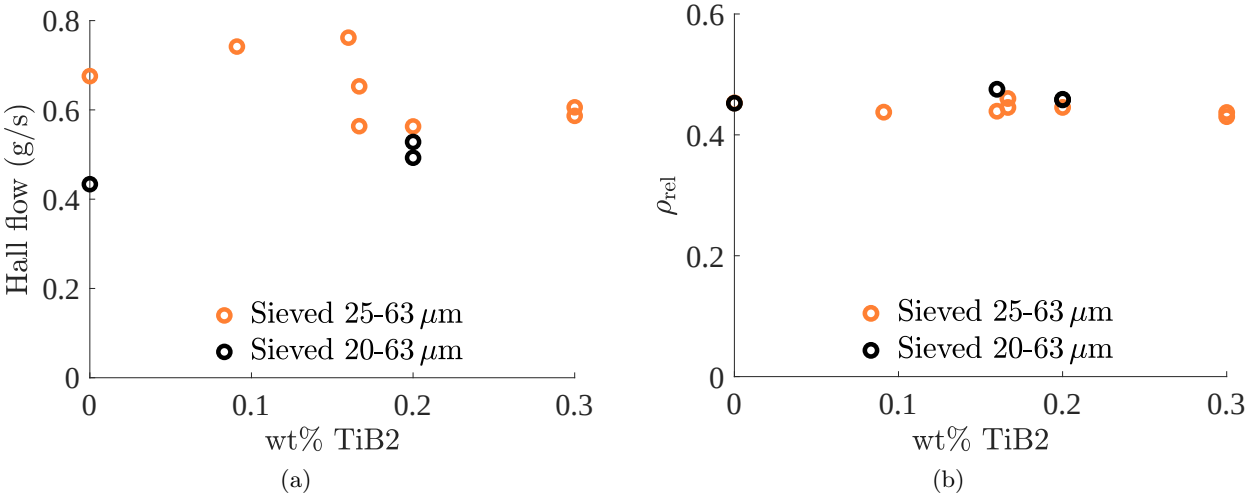

Figure 26. Composite powder performance as a function of ceramic content.

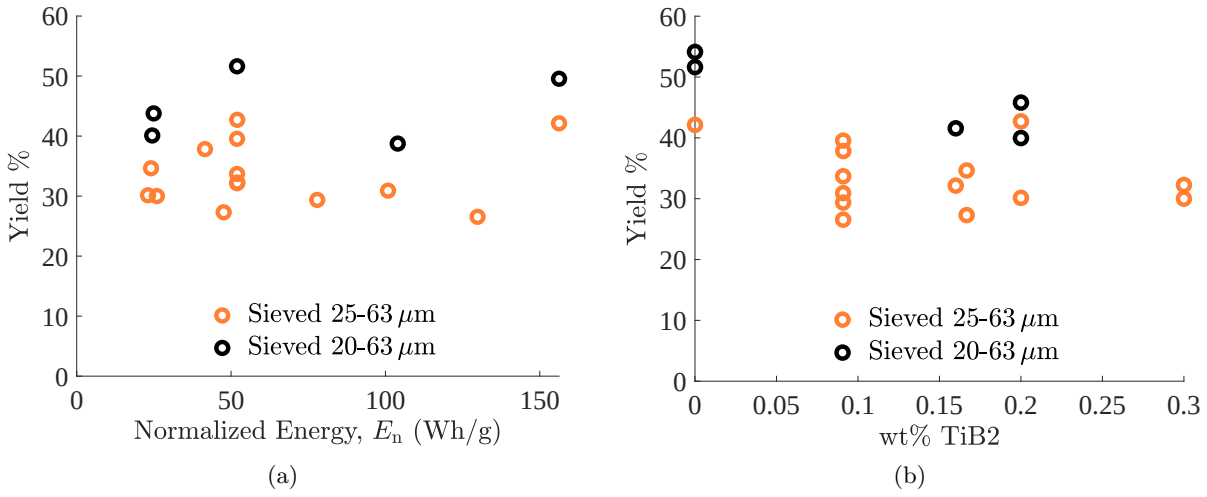

Figure 27. Composite powder yield as a function of E_n and ceramic content.

3. LASER CONSOLIDATION

Laser consolidation is being performed with a custom built SLM testbed from Aconity3D in Germany (Figure 28). Unlike commercial machines, the SLM testbed allows selection of process parameters over a wide range of laser parameters, scan strategies, powder bed temperatures, and recoating parameters. The selection of these parameters is being guided by analytical and numerical models that predict melt pool characteristics and thermal history as a function of process parameters and powder composition.

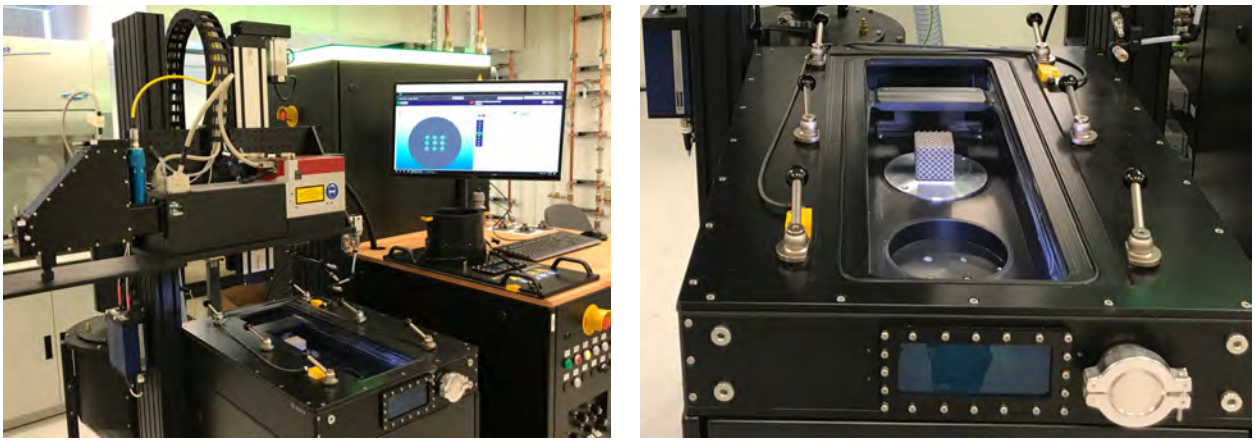

(a) (b)

Figure 28. Aconity SLM research system. (a) Build chamber, CW fiber laser, scan head, and control cabinet; (b) Close-up of build chamber, showing powder supply cylinder, build platform, and powder recoater (front to back).

3.1 DESCRIPTION OF SLM TESTBED

The SLM testbed was installed at MIT LL in 2018. It is an open access system designed to our specifications for the development of new materials for SLM. Process conditions can be broadly tuned to prevent the occurrence of defects and produce desirable microstructures. The testbed's key features include:

- Inert build chamber with recirculation and filtering that enable the processing of highly reactive materials such as aluminum alloys. (Flow rate of inert gas across the build plate is controlled to remove weld fumes and splatter.)

- Continuous wave fiber laser with maximum power of 420 W
- On-the-fly adjustment of laser beam power and diameter (d_{beam}=80–500 μm)
- Full control of the laser scan path
- Powder bed preheating up to 500 °C
- Size reduction kits for the build platform and supply platform (d=55 mm) that enable the processing of small quantities of powder (less than 100 g of powder for a build height of 1 cm)
- Interchangeable recoater blade (steel, rubber, or carbon fiber brush) and full control of powder layer thickness, blade height, and blade velocity
- Melt pool temperature sensing with two pyrometers
- High speed CMOS camera
- Support for additional sensors for process monitoring and addition of feedback control

3.2 LASER CONSOLIDATION OF SINGLE TRACKS OF POWDER

In the first set of experiments with the milled composite powders, single lines were consolidated with the SLM testbed at various laser powers and scan velocities. For a given material, this type of experiment is a highly efficient way to estimate the range of process parameters that can be used to fabricate bulk samples with minimal defects. Within this process window, the single lines, or tracks (similar to laser weld beads), exhibit the following characteristics:

- Smooth, uninterrupted profiles when viewed from above
- Sufficient penetration into the substrate to ensure a strong connection
- Sufficient height above the substrate to build in the vertical direction
- An angle of connection with the substrate of close to 90°

In addition to the determination of laser power and scan velocity, single track experiments can also provide estimates of the optimal hatch spacing and powder layer thickness, based on the dimensions of the weld bead's profile.

We prepared single layer samples by spreading 50 μm layers of gas atomized and composite powder over an AlSi12 substrate using the SLM recoater equipped with a metal blade. Single lines of powder were then consolidated at powers of 95–380 W and scan velocities of 50–2000 mm/s. The scan lines were all 7.5 mm long and were spaced at 1.5 mm intervals. The experimental results demonstrate that smooth, uninterrupted, tracks can be consolidated from powders with ceramic

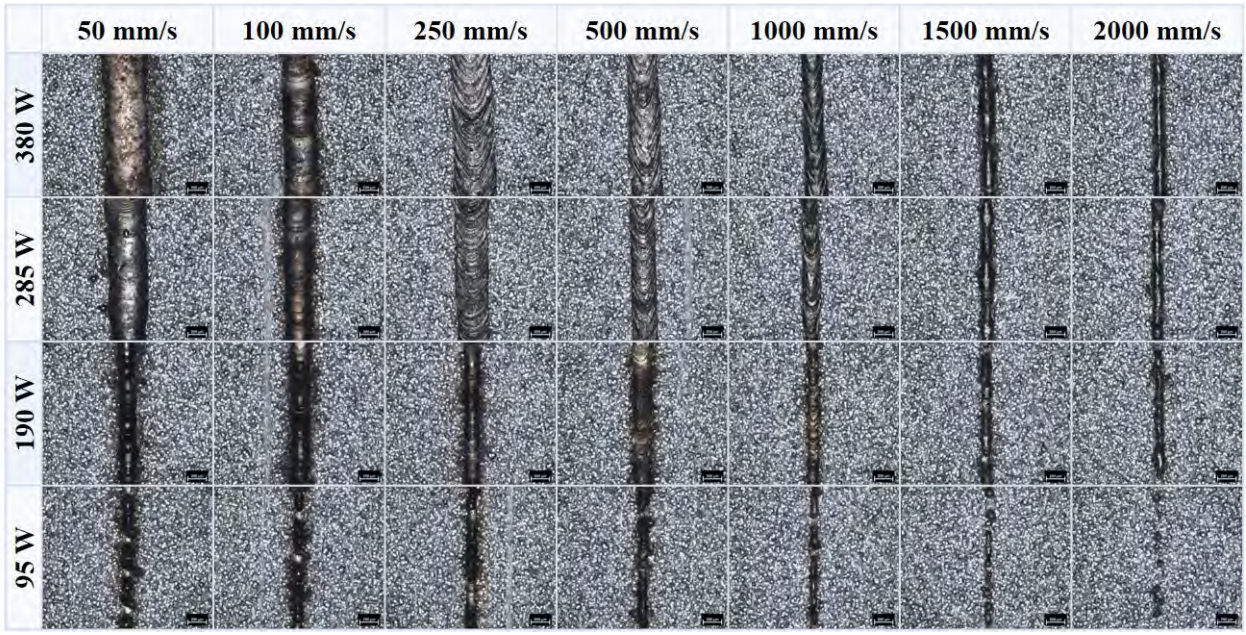

Figure 29. Single track consolidation of plain AlSi10Mg powder, demonstrating the formation of smooth, continuous weld beads.

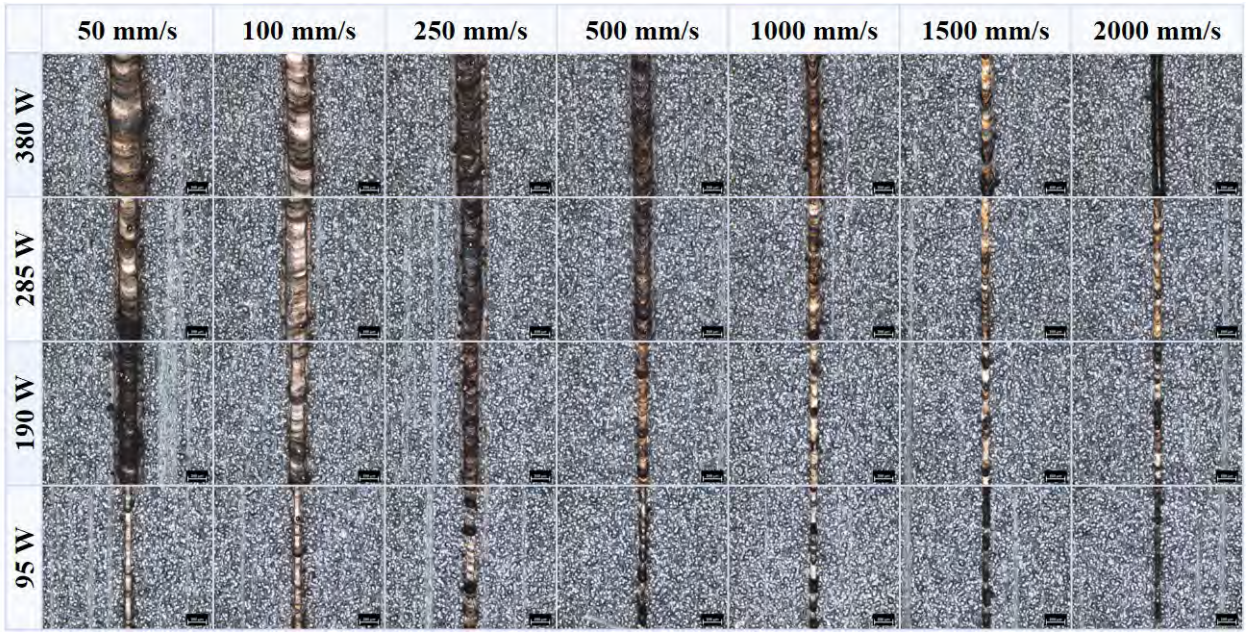

Figure 30. Single track consolidation of composite powder with $w = 10\%$, demonstrating the formation of smooth, continuous weld beads.

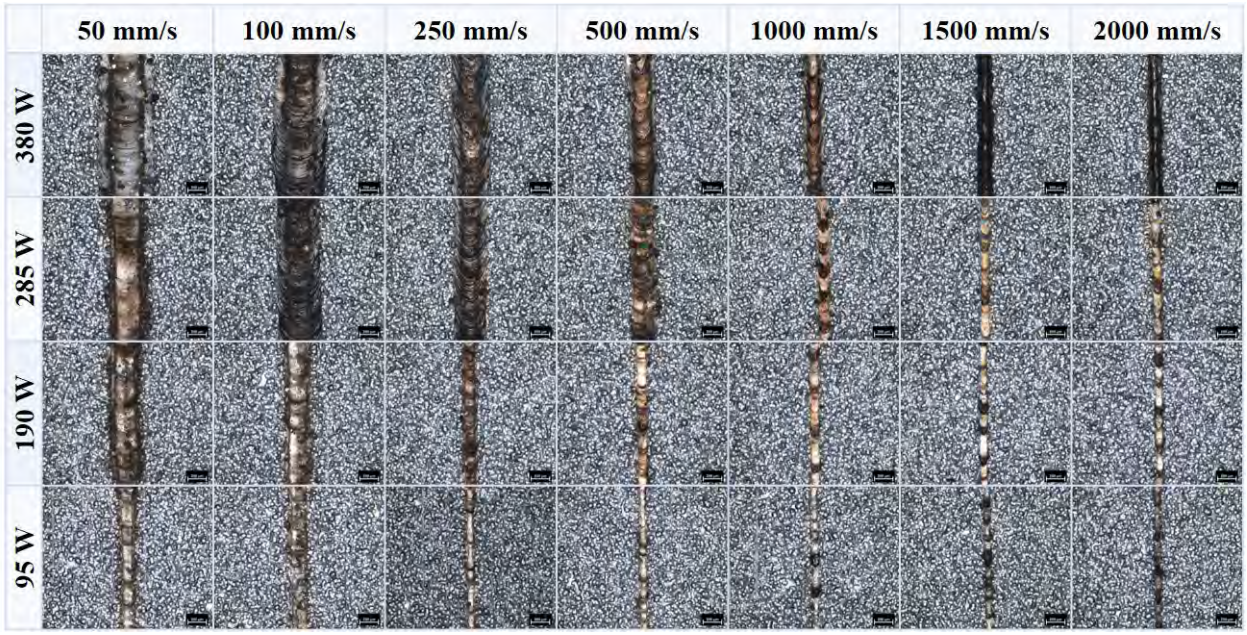

Figure 31. Single track consolidation of composite powder with $w = 16\%$, demonstrating the formation of smooth, continuous weld beads.

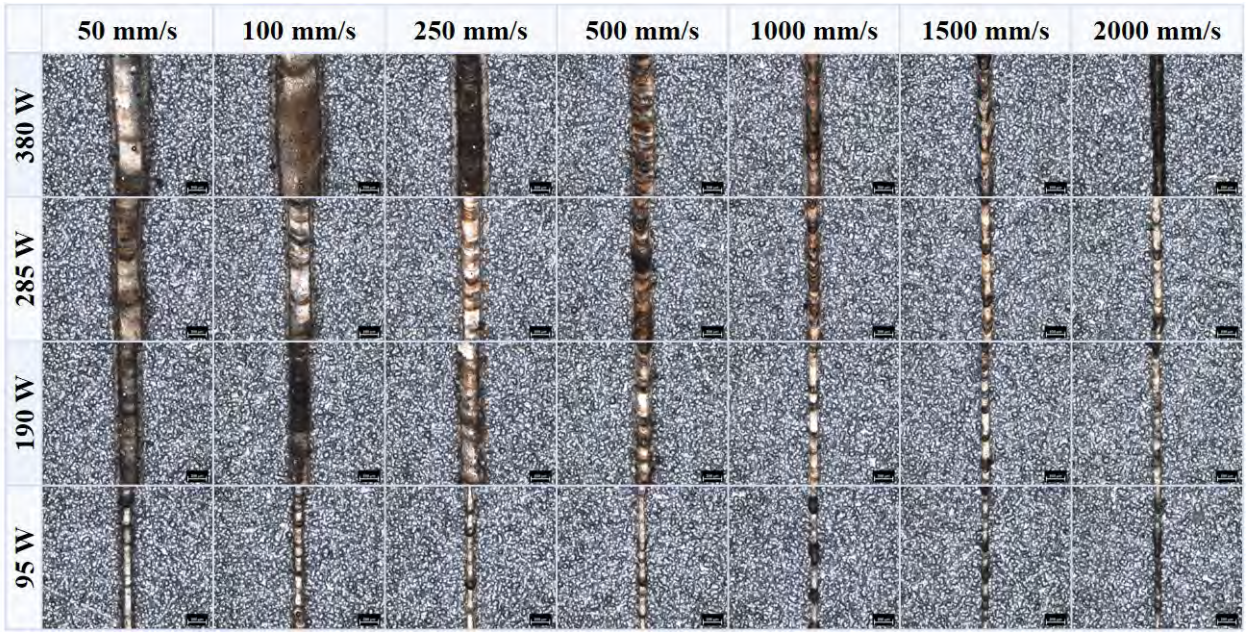

Figure 32. Single track consolidation of composite powder with $w = 30\%$, demonstrating the formation of smooth, continuous weld beads.

contents of up to 30% (Figures 29–32). Therefore, we are confident that defect-free bulk samples and engineering components can ultimately be built from these powders.

The results of the single track consolidation experiments show that the process window for the composite powders comprises laser powers of about 190–380 W at velocities that increase with increasing laser power. Outside this window, at high powers and low velocities, the melt pool transitions from conduction mode to keyhole mode. In keyhole mode, the melt pool temperature exceeds the alloy's boiling point, and evaporation of the liquid metal and high vapor pressures cause a deep channel to form within the melt pool. After the laser passes, the molten metal fills in the channel, leaving behind a flat weld bead and often pores where the channel does not fully close. On the other hand, outside the process window at low powers and high velocities, the consolidated tracks exhibit irregularities and poor connection to the substrate. Here, the melt pool fails to wet the substrate completely because surface tension spheroidizes the liquid metal and the substrate does not melt sufficiently.

Somewhat surprisingly, the laser processing window is not a clear function of the ceramic content of the powder. However, the consolidated tracks do become narrower as the ceramic content of the powder increases, suggesting that the hatch spacing should decrease with increasing ceramic content. We theorize that the reduced width of the tracks is due to an increase in melt pool viscosity caused by the unmelted ceramic particles suspended in the melt pool and/or contamination of the powder by the steel milling media.

3.3 LASER CONSOLIDATION OF BULK SAMPLES (DENSITY CUBES)

Next, we fabricated bulk samples to characterize quantitatively the level of defects in the consolidated composites. In small samples, defects can be caused by keyhole melting, balling of the melt pool, and insufficient remelting of previously consolidated layers. (In larger samples or parts, defects can also be caused by residual stresses.) No matter their cause, however, defects of this type are manifested as porosity in the solid material, which can be measured accurately by the Archimedes method (using samples called "density cubes" because mass density is actually measured). We therefore fabricated $1\,\mathrm{cm}^3$ cubes using various laser powers and scan velocities (Figure 33a).

The process parameters used for the density cubes were selected based on the predicted melt pool dimensions, as well as the results of the single track consolidation experiments: $P = 190{-}380\,\mathrm{W}$, and $v = 500{-}2000\,\mathrm{mm/s}$. The powder layer thickness was $t_{\mathrm{powder}} = 30{-}50\,\mu\mathrm{m}$, and the hatch spacing was $h_{\mathrm{beam}} = 80{-}160\,\mu\mathrm{m}$. The laser scan direction was rotated $\pm 90^\circ$ after each layer, and a 5 mm island scan strategy was used in some cases, meaning that consolidation occurred by 5 mm squares in a checkerboard fashion. After consolidation, the samples were cut off the build plate, and the support structures were removed by milling. The density of each sample was then measured by the Archimedes method (OHAUS Explorer EX), permitting the calculation of the relative density, $\rho_{\mathrm{rel}} \equiv \rho/\rho_{solid} \times 100$. The results show that relative densities of up to 97%

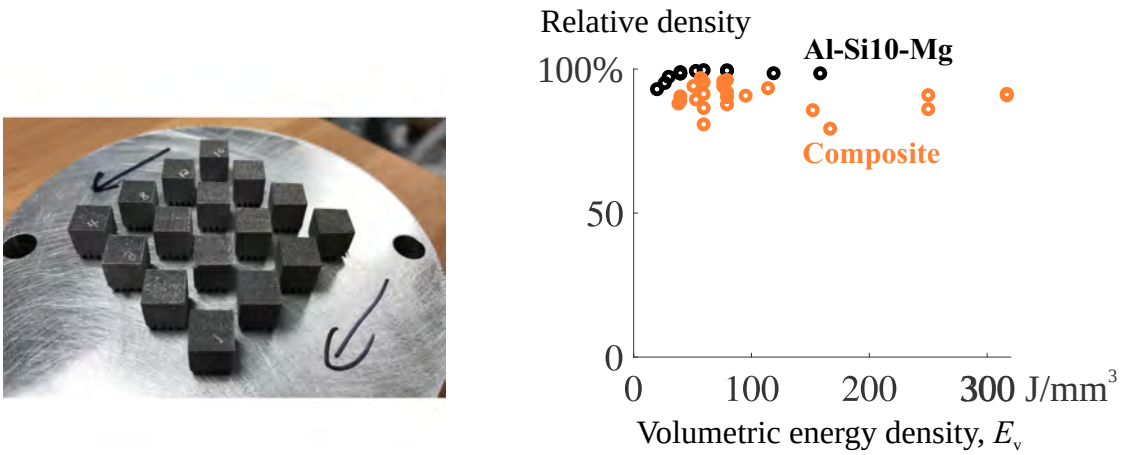

(a) (b)

Figure 33. Laser consolidation of bulk samples of AlSi10Mg. (a) 1 cm^3 density cubes built with P=190–380 W and v=500–2000 mm/s; (b) The relative density of the samples peaks at volumetric energy densities in the range $E_V = 50 - 80$ J/mm^3.

were achieved with the composite powders (Figure 33b). Although energy density is an imperfect measure, it is convenient and common to plot the relative density as a function of the volumetric energy density,

$$E_V = \frac{P}{v\, h_{beam}\, t_{powder}}. \tag{8}$$

For $\rho_{rel} \approx 97\%$, the volumetric energy density is in the range of 50–80 J/mm^3, corresponding to combinations of laser power and scan velocity of ($P = 190$ W, $v = 500$ mm/s), ($P = 285$ W, $v = 1000$ mm/s), and ($P = 380$ W, $v = 1000{-}1500$ m/s). Compared with the results of the single track consolidation experiments, these combinations of power and velocity are all within the determined process window, validating the predictions of the single track experiments.

However, by varying the laser parameters and powder layer thickness, we were unable to reach our goal of 99% relative density. Some tenacious pores still linger, in particular near the melt pool boundaries and at the end of scan vectors. We traced the remaining porosity to two sources related to the milling process: excess hydrogen from the process control agent and iron contamination by the milling media. Hydrogen is the only gas with significant diffusivity in metals and can cause the formation of gas pores during SLM. Iron is known to reduce melt fluidity in Al-Si alloys. Furthermore, iron has very low solid solubility in aluminum and tends to form the brittle intermetallic $\beta - Al_9Fe_2Si_2$ phase, which can block interdendritic feeding and cause shrinkage porosity. The presence of excess hydrogen and iron in the composite powders was confirmed

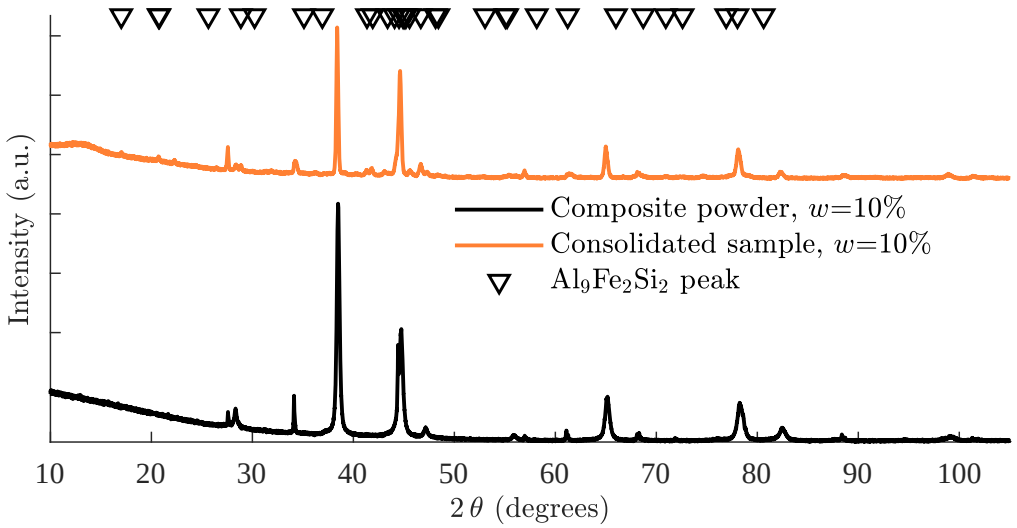

Figure 34. XRD scans of ball-milled composite powder and consolidated composite at w=10%.

by chemical analyses, and XRD identified $\beta - Al_9Fe_2Si_2$ in the consolidated composite material (Figure 34), confirming our suspicions.

The microstructure of the samples was characterized by SEM and optical microscopy. Bulk samples were sectioned both horizontally and vertically with a diamond saw and then mounted, ground, and polished. Away from the aforementioned pores, the microstructure of the consolidated composites is robust and exhibits the desired morphology: small ceramic particles that are well distributed and fully bonded to the matrix metal (Figure 35). At the microscale, away from the pores, the microstructure is uniform and exhibits the fine cell size typical of rapidly solidified aluminum (Figure 36a). At the scale of the ceramic particles, there are no defects, such as cracks or voids initiating at the particles, that would indicate the incompatibility of the two phases. The porosity occurs at the mesocale and appears to be a function of the position within the melt pool and thus the cooling rate and thermal gradient—unrelated to the presence of the ceramic phase (Figure 36b).

At the microscale, the mechanical properties were characterized by instrumented microindentation (Figure 37a). In this test, the resistance to indentation is measured as a function of penetration depth. When the indents are positioned away from the melt pool boundaries, the consolidated composite exhibits an over 40% improvement in modulus and an over 100% improvement in hardness, relative to plain AlSi10Mg (Figure 37b). These enhanced properties are further evidence of the distribution, wetting, and bonding of the ceramic particles.

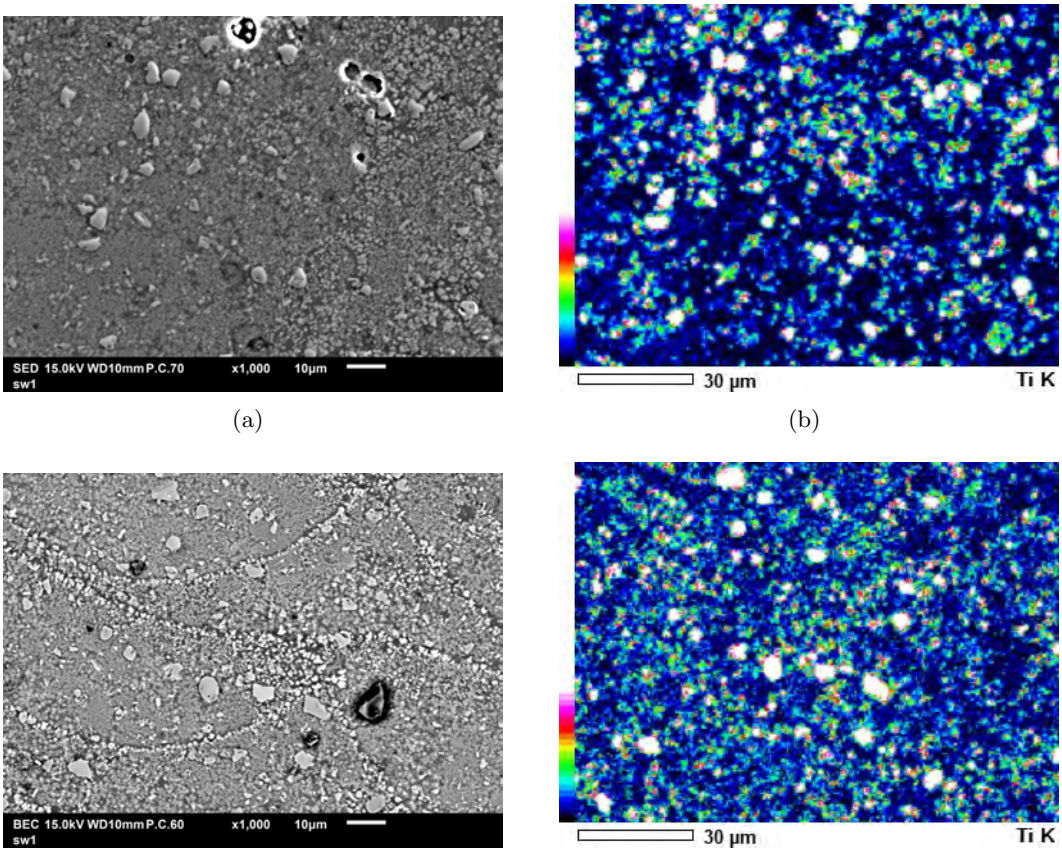

(a) (b)

(c) (d)

Figure 35. Consolidated composite with $w = 16\%$. (a) Secondary electron image of horizontal section at 1000x magnification. (b) EDS map of horizontal section at 1000x magnification. (c) Backscattered electron image of vertical section at 1000x magnification. (d) EDS map of vertical section at 1000x magnification.

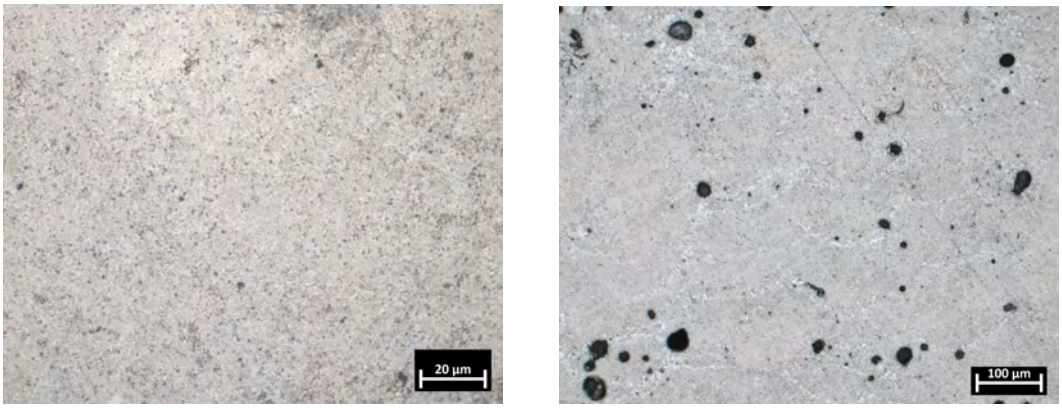

(a) (b)

Figure 36. Consolidated composite with $w = 10\%$. (a) Optical microscope image of horizontal section. (b) Optical microscope image of vertical section.

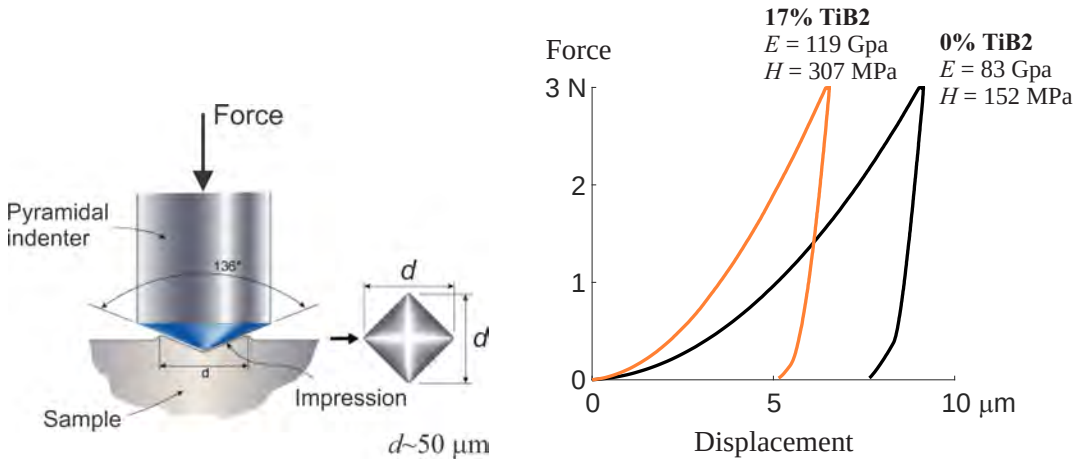

(a) (b)

Figure 37. Measurement of mechanical properties with microindentation. (a) Schematic of method. (b) Load-displacement curves and calculated properties of consolidated materials.

This page intentionally left blank.

4. CONCLUSION

During FY 2019, we made significant progress toward our goal of inventing high performance structural materials for additive manufacturing. We demonstrated that, via ball milling, we can produce composite powders with high ceramic content that flow and pack similarly to plain aluminum powders. To our knowledge, these are the first highly-reinforced composite powders that can be spread in thin, uniform layers by an SLM machine. In the laser consolidation of these powders, we demonstrated the formation of stable melt pools and smooth, continuous fused tracks with ceramic contents as high as 30%. Furthermore, bulk samples exhibited relative densities as high as 97% with an over 40% improvement in stiffness and 100% improvement in hardness at the microscale.

In FY 2020, we will transition these promising material properties from the microscale to the macroscale, proving that useful engineering components can be fabricated from these composite powders. This objective will be accomplished by improving the powder quality so that the process window that results in defect-free consolidation is as wide as possible. Results from the literature and our own preliminary experiments indicate that the sources of defects can be virtually eliminated by a change in milling media and adding an inexpensive post-processing step to the powder fabrication procedure. Once we have eradicated the defects at the mesoscale, we will shift our focus to building larger samples that can be used to measure directly engineering properties such as Young's modulus, yield strength, and elongation in uniaxial tension. Based on these measurements, as well as the characterization of the microstructure, we will tune the ceramic content and consolidation parameters such that the mechanical properties are maximized.

Development of metal matrix composites for SLM will greatly enhance the performance of a wide variety of airborne sensor and communication systems. Structural components fabricated from MMCs will be stiffer and more stable than those fabricated from unreinforced metals, and reductions in structural weight will enable increases in payload capacity. Reducing weight will also alleviate the need for vibration isolation systems, decreasing system weight further and reducing cost. Moreover, the ability to tune material properties by varying ceramic content will enable thermal expansion matching of components. At the conclusion of the program, we envision transferring the materials and processes to production SLM machines at MIT LL and other organizations, thereby opening up many new applications for these impressive, yet currently vastly underused, materials.

An additional benefit of this program is the substantial leave-behind capability which has already been developed that will spur additional research in the area of materials for harsh and extreme environments. We have acquired the equipment and expertise to produce new, novel materials with mechanical alloying that can be consolidated by SLM or a variety of other methods. Mechanical alloying is the ideal method to produce novel, metastable materials such as high entropy alloys, nanocrystalline alloys, refractory materials, and radiation tolerant materials for applications such as hypersonics and nuclear reactors.

This page intentionally left blank.

A RELATED PUBLICATIONS 2019

E. M. Parsons and T. M. Mower, Additive manufacturing of lightweight metal composites, NASA Breakthrough Materials Workshop, Huntsville, AL, April 2019.

E. M. Parsons, Selective laser melting of aluminum-ceramic composites, 30^{th} Annual International Solid Freeform Fabrication Symposium, Austin, TX, August 2019.

E. M. Parsons, Developing feedstock powder for laser consolidation of aluminum metal matrix composites, Materials Science & Technology Technical Meeting, Portland, OR, October 2019.

E. M. Parsons. Lightweight cellular metal composites with zero and tunable thermal expansion enabled by ultrasonic additive manufacturing: Modeling, manufacturing, and testing, *Composite Structures* 223, 2019.

This page intentionally left blank.